MAT-3921

MASTER'S THESIS IN

INDUSTRIAL MATHEMATICS

Multi-fractal Stochastic Modeling of the Auroral Electrojet Index

Martin Jong Yul Shon Sund

December, 2009

FACULTY OF SCIENCE AND TECHNOLOGY
Department of Mathematics and Statistics
University of Tromsø

Master Thesis in Industrial Mathematics

Multi-fractal Stochastic Modeling of the Auroral Electrojet Index

Martin Jong Yul Shon Sund

December 2009

Acknowledgements

I wish to especially thank my advisor, doctoral Martin Rypdal, for introducing me to such an interesting project. It is strange to remember that it all started with talks about sandpiles. Even as the only student that year taking this particular subject, Martin Rypdal always motivated me with many hours of instructive lessons. He has many times helped me with mathematical programming, offered technical notes and made corrections from spelling to more critical errors. I am especially grateful for all the hours of difficult teachings made easily understandable by Rypdal.

I want to thank my advisor, professor Einar Mjølhus, for helping me succeed. If Einar had not been there and believed in my completion of this thesis, then I do not think it would have worked out so well. I am without doubt thankful for all the support and his sharing of long expertise, over many sessions. I am fortunate to be been guided by such highly appreciated advisors.

Finally, I give my special thanks to Silje-Linn for all her invaluably support and belief in me at all times. She has been an irreproachable life partner at many long days and late evenings when working. At all times she has brighten with a cheerful and motivating spirit. Without her reliable presence I would not have been able to continue.

Figure 0.1: Cite: "The front of the new Norwegian bank note shows a portrait of Kristian Birkeland against a stylized pattern of the aurora and a very large snowflake. Birkeland's terrella experiment, which consisted of a small, magnetized sphere representing the Earth suspended in an evacuated box, is shown on the left. When subjected to an electron beam a glow of light would appear around the magnetic poles of the terrella, simulating the aurora. The back of the note shows a geographic map of the north polar regions including Scandinavia on the right and northern Canada on the bottom. A ring encircling the magnetic dip pole (located near Resolute, Canada) symbolizes the location of auroral phenomena including the satellite-determined statistical location of Birkeland currents. Birkeland's original depiction of field-aligned currents published in 1908 is shown in the lower right corner" [17].

Abstract

In this thesis we have analyzed the Auroral Electrojet (AE) Index over the years 2000 to 2005, a time series consisting of over 3 000 000 data points. The aim is to describe this data as a multi-fractal stochastic process. We first introduce a class of random multiplicative measures, which provide the multi-fractality in the stochastic processes that will be defined later. We also review the theory of fractal dimensions and scaling functions, before introducing the Multifractal Model of Asset Returns (MMAR), [15].

The scaling properties of various versions of the MMAR model are compared with the scaling function of the AE Index, and through this we describe the multi-fractal properties of the AE Index.

Additionally, we have studied probability density functions (pdf) at different time scales, and used this to compare the stochastic models with the AE data.

Finally we have tested our diagnostic tools on simulated multi-fractal models. These experiments show that the methods are capable of detecting multi-fractality. The results are good if we average over several independent realizations of the processes.

Contents

1 Introduction

An elctrojet is an electric current in the E-region of the Earth's ionosphere. They are generally divided into the Equatorial Elecrojet, above the magnetic equator, and the Auroral Electrojets (AE) near the northern and southern polar circles. The AE currents are carried primarily by electrons at altitudes from 100 to 150 km.

The AE Index is derived from geomagnetic variations in the horizontal component of the magnetic field observed at selected observatories along the auroral zone in the northern hemisphere. It is recorded with 1 minute resolution. Until 2004, the AE Index was derived from 12 magnetometers, with five of them lying north of the Arctic Circle, see figure Appendix 6.1 [21], [13]. The data is normalized for each station by averaging the data of the five international quietest days of the month. Then among the data from all the stations at each given universal time (UT), the largest and smallest values are selected. The difference of the largest (AU) and the smallest (AL) values defines the AE Index. The AU and AL indices are intended to express the strongest current intensity of the eastward and westward auroral electrojets respectively. Thus the AE Index represents the overall activity of the electrojets [13], [5].

The influence of the solar wind plasma and the interplanetary magnetic field on the magnetosphere is a central theme in solar-terrestrial physics. The AE Index is now widely used by researches in physics, aeronomy, studies of sub-storm morphology, the behavior of communication satellites, radio propagation and scintillation, and the coupling between the interplanetary magnetic field and the Earth's magnetosphere [10]. Moreover there is an ongoing debate whether global climatic changes are related to the sun spot activity. The AE Index provides information which is central to this question.

In this thesis we study the fluctuations of the AE Index on time scales up to 10^2 minutes. These are called the sub-storm scales, and the fluctuations we investigate are belived to characterize the complex internal dynamics of the magnetosphere.

When studying the dynamics of complex systems such as the magnetosphere, we are primeraly interested in extracting robust characteristics of the underlying dynamics. We will investigate the stochastic properties using fractal modeling and try to classify the structure of the family of probability density functions.

It is interesting to note that the models we apply to investigate the AE Index actually are borrowed from the modern theory of financial time series. The development of this theory started with Bachelier (1900) [1] who focused on independent and normal distributed fluctuations as a probabilistic description of financial prices. Actual data tend though to have temporal dependence. Also, the tails of the pdfs of observed data are found to exhibit fatter tails than a normal distribution.

Later with Engle (1982) [8] and Bollerslev (1986) [3] models such as ARCH/ GARCH became popular. Developments like FIGARCH (Baillie, Bollerslev and Mikkelsen (1996) [2]) took the models closer to the actual financial data.

Multi-fractal measures were introduced in Mandelbrot (1972) [14] and have been applied to many physical phenomena such as the distribution of turbulent dissipation, stellar matter,

mineral composition and much more. Recently, multi-fractals have also been proposed as a description of finacial data. Multifractality can be seen as a property of certain measures, and combining such measures with self-similar stochastic processes produce so-called multi-fractal processes. Therefore, multifractality will be referred to both measures and processes depending on the object at hand. The Multifractal Model of Asset Returns (MMAR) of Mandelbrot [15], is a spesific class of stochastic processes designed to describe multifractality in financial time series. We will try to investigate whether the MMAR model gives a useful description of the AE Index. Through construction of scaling functions we want to determine the multifractality of the AE Index. Further we will look at probability density functions (pdf) and compare theoretical results for our models with estimated pdfs in the AE Index. As an inspection we will study synthetic data to see if we can accurately estimate scaling functions.

The thesis is structured as follows: In section 2 we introduce the simplest multi-fractal measure, a Bernoulli measure. An extension to Markov measures follows. Then we will look at singularity spectra of measures and curves. In section 3 we introduce probability density functions. We analyse the AE Index and apply the tools we have introduced so far. In the last section we test our diagnostic tools on simulated MMAR models.

We remark that the MMAR model is a composition of a fractional Brownian motion with the distribution function of a random measure on the real line. In the construction of Mandelbrot, this random measure is a so-called log-normal multiplicative cascade. In order to better describe the AE Index we have modified the construction so that the multifractality is given by randomized Bernoulli measures or randomized Markov measures. We briefly consider log-normal cascades in section 3.2.

2 Multi-fractal Stochastic Processes

In this section we introduce the stochastic processes that will be considered in this thesis. We begin by constructing and randomizing multi-fractal measures on the interval. In sections 2.3-2.6 we use these random measures to define multi-fractal stochastic processes.

2.1 The Iterative Multiplicative Binomial Measure

The binomial measure, the Bernoulli measure or sometimes the Besicovitch measure, is the simplest multi-fractal measure on the interval $I = [0, 1]$. We construct an iterated function system defined by maps $g_1, ..., g_N : I \to I$. Where $g_i = a_i x + b_i$ with $a_i \in (0, 1)$ and $\text{int}(g_i(I)) \cap \text{int}(g_j(I)) = \emptyset$ for $i \neq j$. We choose:

$$g_i = \frac{x}{N} + \frac{i-1}{N}.$$

Define $\Delta_{i_1,...,i_n} = g_1 \circ ... \circ g_n(I)$. Let $\Sigma_N^+ = \{1, ..., N\}^{\mathbb{N}} = \{(i_1 i_2 i_3 ...) | i_k \in \{1, ..., N\}\}$ and $\chi : \Sigma_N^+ \to I$ be given by

$$\chi : \underline{i} = (i_1 i_2 i_3 ...) \mapsto \text{ unique element of } \bigcap_{n \geq 1} \Delta_{i_1,...,i_n}. \tag{2.1}$$

The map χ is continuous, so we can construct a Borel measure ν on I by choosing a Borel measure μ on Σ_N^+. Let $\nu = \chi_* \mu$ i.e.

$$\nu(\Delta_{i_1,...,i_n}) = \mu(\chi^{-1}(\Delta_{i_1,...,i_n})) = \mu([i_1 ... i_n]),$$

where

$$[i_1 \cdots i_n] = \left\{ \underline{j} \in \Sigma_N^+ | j_1 = i_1, ..., j_n = i_n \right\}$$

is the cylinder of the finite sequence $i_1, ..., i_n$. We choose numbers $P_1, ..., P_N \in (0, 1)$ where $P_1 + ... + P_N = 1$ and define measures by

$$\nu(\Delta_{i_1,...,i_n}) = \mu([i_1 ... i_n]) = P_{i_1} \cdots P_{i_n}.$$

Given μ (does not have to be a Bernoulli measure) we can construct a random measure. Let $\mathcal{T}_N$ be the set of all sequences on the form

$$\underline{k} = (k_1 ... k_N k_{11} ... k_{1N} ... k_{21} ... k_{2N} ... k_{NN} k_{111} ...)$$

where $k_{i_1 ... i_n} \in \{1, ..., N\}$, and for all $i_1, ..., i_n : \{k_{i_1 ... i_n} | i_k = 1, ..., N\} = \{1, ..., N\}$. Then $\{[k_{i_1} k_{i_1 i_2} ... k_{i_1 ... i_n}] \, | i_k = 1, ..., N\} = \{[i_1 \cdots i_n] \, | i_k = 1, ..., N\}$, and $\mathcal{T}_N \simeq \Sigma_{N!}^+$. We can now let the uniform Bernoulli measure on $\Sigma_{N!}^+$ induce a probability measure u on $\mathcal{T}_N$. Letting $\mathcal{M}(I)$ be the space of Borel probability measures on the interval I, we define a random measure:

$$\begin{array}{c} (\mathcal{T}_N, \mathcal{B}, u) \to \mathcal{M}(I) \\ \underline{k} \to \nu_{\underline{k}} \end{array} \tag{2.2}$$

where $\nu_{\underline{k}} = \chi_* \mu_{\underline{k}}$ and $\mu_{\underline{k}}([i_1 ... i_n]) = \mu([k_{i_1} k_{i_1 i_2} ... k_{i_1 ... i_n}])$.

For a Bernoulli measure with $N = 2$ the construction is as follows:

At stage $k = 0$ we start with the uniform probability measure μ_0 on $I = [0, 1]$. In step $k = 1$, the measure μ_1 uniformly spreads mass P_1 on the subinterval $\Delta_1 = \left[0, \frac{1}{2}\right]$ and mass P_2 on subinterval $\Delta_2 = \left[\frac{1}{2}, 1\right]$. In the next step, $k = 2$, the subinterval $\Delta_1 = \left[0, \frac{1}{2}\right]$ is split into two subintervals $\Delta_{11} = \left[0, \frac{1}{4}\right]$ and $\Delta_{12} = \left[\frac{1}{4}, \frac{1}{2}\right]$, each given a fraction (P_1 and P_2) of the mass P_1. The same procedure is applied to the subinterval $\Delta_2 = \left[\frac{1}{2}, 1\right]$. We obtain:

$$\mu_2\left(0, \left[\frac{1}{4}\right]\right) = P_1 P_1 \quad , \quad \mu_2\left(\left[\frac{1}{4}, \frac{1}{2}\right]\right) = P_1 P_2 \quad , \quad \mu_2\left(\left[\frac{1}{2}, \frac{3}{4}\right]\right) = P_2 P_1 \quad , \quad \mu_2\left(\left[\frac{3}{4}, 1\right]\right) = P_2 P_2.$$

Iterating this procedure generates an infinite sequence of measures.

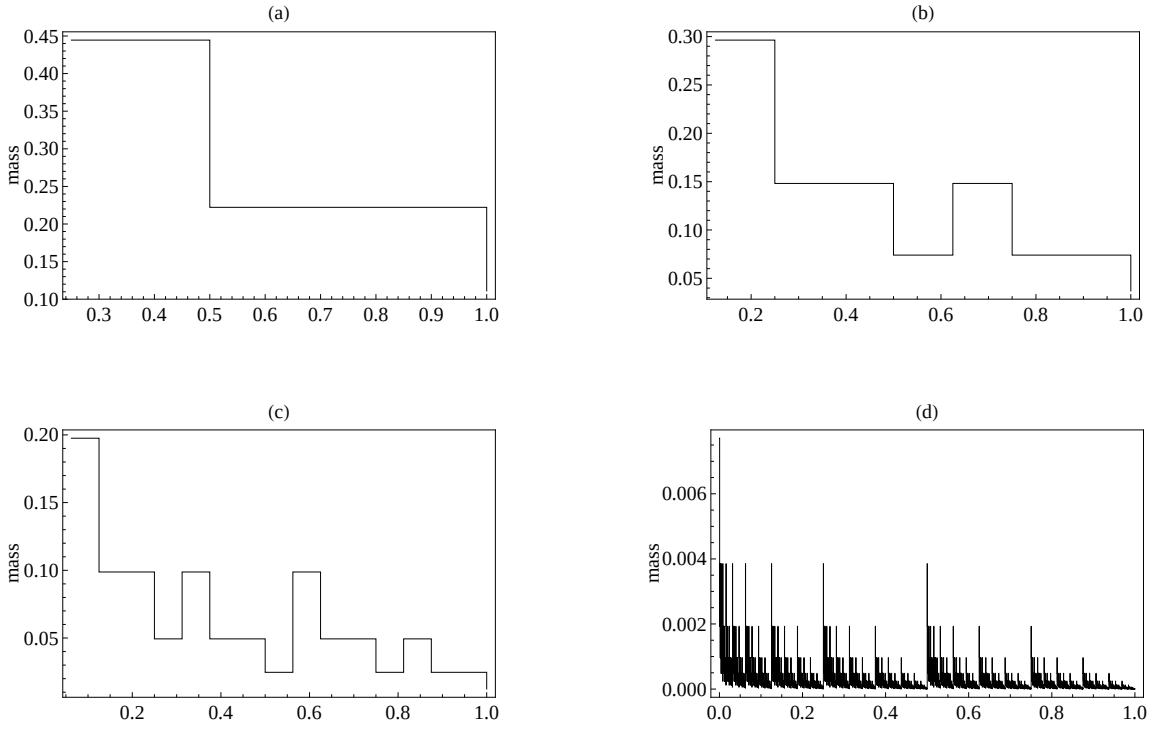

Figure 2.1: Densities of a simple iterated procedure with probabilities $P_1 = 1/3$ and $P_1 = 2/3$. $N = 2$. (a): Iteration $k = 2$. (b): Iteration $k = 3$. (c): Iteration $k = 4$. (d): Iteration $k = 12$.

The limit of this infinite sequence is a binomial measure (or a Bernoulli measure on the interval). A simple binomial measure is illustrated in figure 2.1. The binomial measure is a singular probability measure since it has no density. Because of the relation $P_1 + P_2 = 1$, and noting that each stage of the multiplicative cascade preserves the mass, we call the procedure conservative.

Instead of choosing the allocation of mass in a strict deterministic way, we can extend the procedure to include randomness. At each subinterval in the iterated procedure the mass is distributed using a random "treestructure", breaking down the intervals according to the random element $\underline{k} \in \mathcal{T}_N$. This is further explained by M. Rypdal (2009) [19] and discussed in assignment by M.S. (2009) [20]. An example of a random Bernoulli measure is shown in figure 2.2.

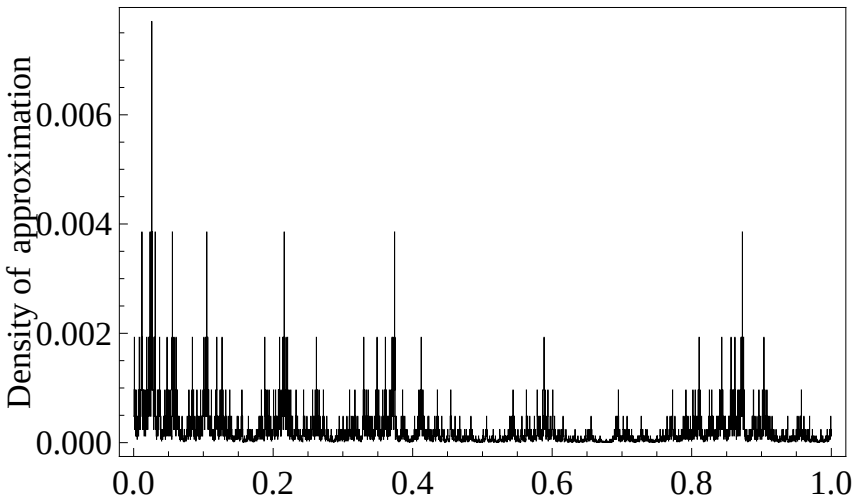

Figure 2.2: Random measure with iteration $k = 11$.

2.1.1 Generalization to Markov Measures

Further extensions can be to consider a Markov measure μ_{M}. Let $\|\pi_{ij}\|$ be a $N \times N$ matrix with $\pi_{ij} \in (0,1)$ and for all $j : \sum_j \pi_{ij} = 1$. Let $P = (P_1, ..., P_N)^T$ be a normalized $(P_1 + ... + P_N = 1)$ eigenvector of π^T and define the measure as:

$$\nu_{\mathrm{M}}(\Delta_{i_1,\cdots,i_n}) = \mu_{\mathrm{M}}([i_1, ..., i_n]) = P_{i_1}\pi_{i_1 i_2}\pi_{i_2 i_3}\cdots\pi_{i_{n-1} i_n}. \tag{2.3}$$

The randomization of a Markov measure follows 2.2.

2.2 The Multi-fractal Spectrum

A multi-fractal object can be caracterized by its so-called singularity spectrum. For measures, this spectrum consists of the Hausdorff dimensions of the level sets of the pointwise dimensions. For curves, such as the realzations of a stochastic process, the singularity spectrum is constructed from the Hausdorff dimensions of the level sets of the local Hölder exponents. We start by considering the multi-fractal spectrum of a Bernoulli measure on the interval.

2.2.1 Hausdorff dimension

The Hausdorff-Besicovitch dimension is defined as follows: For $Z \subseteq \mathbb{R}$, let

$$m_\alpha(Z) = \lim_{\epsilon \to 0} \quad \inf_{\text{diam}(\mathcal{U}) \leq \epsilon} \quad \sum_{U \in \mathcal{U}} \text{diam}(U)^\alpha$$

where the infimum is taken over all open covers of Z with diameter $\leq \epsilon$.

Assume that $m_\alpha(Z) < +\infty$. Let $\beta > \alpha$. Then

$$\begin{aligned} m_\beta(z) &= \lim_{\epsilon \to 0} \quad \inf_{\text{diam}(\mathcal{U}) \leq \epsilon} \quad \sum_{U \in \mathcal{U}} \text{diam}(U)^\alpha \text{diam}(U)^{\beta - \alpha} \\ &\leq \lim_{\epsilon \to 0} \quad \epsilon^{\beta - \alpha} \inf_{\text{diam}(\mathcal{U}) \leq \epsilon} \quad \sum_{U \in \mathcal{U}} \text{diam}(U)^\alpha = 0. \end{aligned}$$

This shows that there exists a number α_c such that $m_\alpha(Z) = +\infty$ for $\alpha < \alpha_c$ and $m_\alpha(Z) = 0$ for $\alpha > \alpha_c$. The Hausdorff dimension is:

$$\dim_H(z) = \alpha_c = \inf \{\alpha \mid m_\alpha(z) = 0\}.$$

For a Borel measure ν on $\mathbb{R}$ the pointwise dimensions are

$$d_\nu(x) = \lim_{\epsilon \to 0} \frac{\log \nu(B_\epsilon(x))}{\log \epsilon},$$

where $B_\epsilon(x)$ is a ϵ-ball centered in x.

Actually we consider the upper and lower limits: $\overline{d}_\nu(x) = \overline{\lim}_{\epsilon \to 0} \frac{\log \nu(B_\epsilon(x))}{\log \epsilon}$ and $\underline{d}_\nu(x) = \underline{\lim}_{\epsilon \to 0} \frac{\log \nu(B_\epsilon(x))}{\log \epsilon}$. If $\overline{d}_\nu(x) \neq \underline{d}_\nu(x)$ then the pointwise dimension is not defined at x, and x is considered an irregular point.

The multi-fractal spectrum of the measure ν is:

$$f_\nu(\alpha) = \dim_H \{x \in \mathbb{R} \mid d_\nu(x) = \alpha\}$$

where $\dim_H$ denotes Hausdorff dimension.

M. Rypdal (2009) [19] gives a detailed explanation of how to calculate the multi-fractal spectrum of a Bernoulli-measure. Let $N = 2$ for simplicity. We will consider μ_q to be a Bernoulli measure on Σ_2^+ which induces a measure $\nu_q = \chi_* \mu_q$ on the interval. The measure μ_q is defined by the probabilities

$$\begin{aligned} P_1^{(q)} &= \lambda_1^T P_1^q \\ P_2^{(q)} &= \lambda_2^T P_2^q, \end{aligned}$$

where P_1, P_2 are the probabilities that define μ, and λ_1, λ_2 are the contraction rates for the iterated function system that define the map $\chi : \Sigma_2^+ \to I$. We must require that:

$$P_1^{(q)} + P_2^{(q)} = 1.$$

This can be written as

$$\lambda_1^T P_1^q + \lambda_2^T P_2^q = 1. \tag{2.4}$$

Clearly T is dependent on q. We differentiate equation 2.4 and obtain

$$-T'(q) = \frac{(\log P_1)P_1^{(q)} + (\log P_2)P_2^{(q)}}{(\log \lambda_1)P_1^{(q)} + (\log \lambda_2)P_2^{(q)}}.$$

Let $\hat{P}$, $\hat{\lambda}$: $\Sigma_2^+ \to \mathbb{R}$ be the simple functions $\hat{P}(\underline{i}) = P_{i_1}$ and $\hat{\lambda}(\underline{i}) = \lambda_{i_1}$ respectivly. Then the following holds:

$$\begin{aligned}\int \log \hat{P} d\mu_q &= \log P_1 \mu_q([1]) + \log P_2 \mu_q([2]) \\ &= (\log P_1)P_1^{(q)} + (\log P_2)P_2^{(q)}.\end{aligned}$$

This gives

$$-T'(q) = \frac{\int \log \hat{P} d\mu_q}{\int \log \hat{\lambda} d\mu_q}.$$

The measures μ_q are Bernoulli measures, and all Bernoulli measures are ergodic with respect to the shift map. Thus we can apply Birkhoff's theorem:

$$\begin{aligned}\int \log \hat{P} d\mu_q &= \lim_{n\to+\infty} \frac{1}{n} \sum_{k=0}^{n-1} \log \hat{P}(\sigma^k \underline{i}) \\ &= \lim_{n\to+\infty} \frac{1}{n} \sum_{k=0}^{n-1} \log P_{i_k}\end{aligned}$$

for μ_q-almost all $\underline{i} \in \Sigma_2^+$, where $\sigma : \Sigma_2^+ \to \Sigma_2^+$ is the (forward) shift map defined by:

$$\sigma(i_1 i_2 i_3 \ldots) = (i_2 i_3 \ldots).$$

Hence, for μ_q-almost all $\underline{i} \in \Sigma_2^+$, we have

$$\begin{aligned}-T'(q) &= \frac{\int \log \hat{P} d\mu_q}{\int \log \hat{\lambda} d\mu_q} \\ &= \lim_{n\to+\infty} \frac{\sum_{k=0}^{n-1} \log P_{i_k}}{\sum_{k=0}^{n-1} \log \lambda_{i_k}} \\ &= \lim_{n\to+\infty} \frac{\log P_{i_1} \cdots P_{i_n}}{\log \lambda_{i_1} \cdots \lambda_{i_n}} \\ &= \lim_{n\to+\infty} \frac{\log \mu([i_1 \ldots i_n])}{\log \operatorname{diam}(\Delta_{i_1 \ldots i_n})} \\ &= \lim_{n\to+\infty} \frac{\log \nu([\Delta_{i_1 \ldots i_n}])}{\log \operatorname{diam}(\Delta_{i_1 \ldots i_n})} \\ &= \lim_{n\to 0} \frac{\log \nu(B_\epsilon(\chi(\underline{i})))}{\log \epsilon} = d_\nu(\chi(\underline{i})).\end{aligned}$$

We define $\alpha(q) = -T'(q)$ and $K_{\alpha(q)} = \{x \in I \mid d_\nu(x) = \alpha(q)\}$, where $x = \chi(\underline{i})$. It follows that $\nu_q(K_{\alpha(q)}) = 1$. Next we observe that for $\chi(\underline{i}) \in K_{\alpha(q)}$:

$$\begin{aligned}
d_{\nu_q}(\chi(\underline{i})) &= \lim_{n\to+\infty} \frac{\log \nu(\Delta_{i_1\ldots i_n})}{\log \operatorname{diam}(\Delta_{i_1\ldots i_n})} \\
&= \lim_{n\to+\infty} \frac{\log P_{i_1}^{(q)} \cdots P_{i_n}^{(q)}}{\log \lambda_{i_1} \cdots \lambda_{i_n}} \\
&= \lim_{n\to+\infty} \frac{\log(\lambda_{i_1}^T P_{i_1}^{(q)}) \cdots (\lambda_{i_n}^T P_{i_n}^{(q)}))}{\log \lambda_{i_1} \cdots \lambda_{i_n}} \\
&= T + q \lim_{n\to+\infty} \frac{\log P_{i_1} \cdots P_{i_n}}{\log \lambda_{i_1} \cdots \lambda_{i_n}} \\
&= T + q d_\nu(x) \\
&= T + q\alpha(q).
\end{aligned}$$

Since $\nu_q(K_{\alpha(q)}) = 1$ and $d_{\nu_X(x)} = T + q\alpha(q)$ for all $x \in K_{\alpha(q)}$, we must have $\dim_H K_{\alpha(q)} = T + q\alpha(q)$. This actually follows from a theorem of L. S. Young [16]. To summarize:

$$\begin{aligned}
\dim_H K_{\alpha(q)} = f(\alpha(q)) &= T(q) + q\alpha(q) \\
\alpha(q) &= -T'(q) \\
\lambda_1^{T(q)} P_1^q + \lambda_2^{T(q)} P_2^q &= 1.
\end{aligned} \tag{2.5}$$

We note that $T(q)$ is known as a scaling function of the measure. $f(\alpha)$ is related to T by a Legendre transform $f_\nu(\alpha(q)) = T_\nu(q) + q\alpha(q)$.

2.3 Multi-fractal Time

We will now demonstarte how a random multi-fractal measure can be used to construct a multi-fractal stochastic process. We begin by constructing a process $\{\Theta_\mu(t) \mid t \in [0,1]\}$. This process will be called the multi-fractal time, and it is defined by

$$\begin{aligned}
\Theta_\mu(t) &: (\mathcal{T}_N, \mathcal{B}, u) \to \mathbb{R} \\
\Theta_\mu(t)(\underline{k}) &= \nu_{\underline{k}}([0,t])
\end{aligned}$$

where $(\mathcal{T}_N, \mathcal{B}, u)$ are defined as in section 2.1.

We define the structure function of the stochastic process $\{\Theta_\mu(t)\}$:

$$S_q(\Delta t) = E\left[\Theta_\mu(\Delta t)^q\right].$$

For $\Delta t = N^{-n}$ we observe that:

$$\begin{aligned} E\left[\Theta_\mu(\Delta t)^q\right] &= \int \nu_{\underline{k}}([0,\Delta t])^q dx(\underline{k}) \\ &= \frac{1}{N^n} \sum_{k_1,k_{11},\ldots,k_{1\ldots1}} \mu_{\underline{k}}\left([1\ldots1]\right)^q \\ &= \frac{1}{N^n} \sum_{k_1,k_{11},\ldots,k_{1\ldots1}} \mu\left([k_1 k_{11}\ldots k_{1\ldots1}]\right)^q \\ &= \frac{1}{N^n} \sum_{i_1,i_2,\ldots,i_n} \mu_{\underline{k}}\left([i_1 i_2\ldots i_n]\right)^q. \end{aligned}$$

Define a scaling function $\zeta_{\Theta_\mu}(q)$ by $E\left[\Theta_\mu(\Delta t)^q\right] \sim d(q)\Delta t^{\zeta_{\Theta_\mu}(q)}$ and observe that:

$$\begin{aligned} \zeta_{\Theta_\mu}(q) &= \lim_{n\to\infty} \frac{\log E\left[\zeta_{\Theta_\mu}\left(\frac{1}{N^n}\right)^q\right]}{\log N^{-n}} \\ &= \lim_{n\to\infty} \frac{-n\log N + \log \sum_{i_1,\ldots,i_n} \mu\left([i_1\ldots i_n]\right)^q}{-n\log N} \\ &= 1 + T_\nu(q) = 1 + \frac{1}{q-1} D_q(\chi_*\mu), \end{aligned}$$

where $D_q(\nu)$ is the Hentschel-Procaccia dimension spectrum as mentioned by Pesin [16].

The structure functions $S_q(\Delta t) = E\left[\Theta(\Delta t)^q\right]$ and scaling functions $\zeta(q)$ are important constructions for analysis of mulit-fractal stochastic processes. We will discuss these objects in more detail in the following sections.

2.4 Multifractality

A self-similar stochastic process $\{X(t)|t \geq 0\}$ satisfy the scaling rule:

$$X(ct) \overset{d}{=} c^H X(t),$$

where $\overset{d}{=}$ denotes equality in distribution.

When considering multi-fractal processes one must generalize this relationship. We assume there exists an independent process $\{M(c)\}$ that satisfies:

$$X(ct) \overset{d}{=} M(c)X(t). \tag{2.6}$$

A self-similar process will then satisfy $M(c) = c^H$. With stationary increments, the scaling become:

$$X(t + c\Delta t) - X(t) \overset{d}{=} M(c)\left[X(t+\Delta t) - X(t)\right].$$

We require that if $0 < a, b \leq 1$ the process M takes positive values and the random scaling factors satisfy:

$$M(ab) \stackrel{d}{=} M_1(a)M_2(b),$$

where M_1 and M_2 are independent copies of M. Assuming the expectation is finite we get $E[M(ab)^q] = E[M(a)^q]E[M(b)^q]$ for all $q \geq 0$. With finite moments, the process M satisfies:

$$E[M(c)^q] = c^{\zeta(q)}.$$

Under these conditions we say that $X(t)$ has scaling-properties. We then have

$$\begin{aligned} E\left[|X(\Delta t)|^q\right] &= E\left[|M(\Delta t)|^q\right]\ E\left[|X(1)|^q\right] \\ &= c(q)\Delta t^{\zeta(q)}, \end{aligned} \tag{2.7}$$

with $c(q) = E\left[|X(1)|^q\right]$.

We will later consider a more detailed explanation of the scaling function $\zeta(q)$. A self-similar process, such as a fractional Brownian motion, is mono-fractal with scaling function $\zeta(q) = Hq$. Thus it is a linear function. Brownian motion gives $\zeta(q) = q/2$.

According to Mandelbrot (1997) [15] a multi-fractal stochastic process may be defined as the following:

Definition 2.1. *A stochastic process $\{X(t)\}$ is called multi-fractal if it has stationary increments and satisfies:*

$$E([|X(\Delta t)|^q]) = c(q)\Delta t^{\zeta(q)} \text{ , for all } t \in \mathcal{T},\ q \in \Phi$$

where $\mathcal{T}$ and Φ are intervals on the real line, $\zeta(q)$ and $c(q)$ are functions with domain Φ. Moreover, we assume that $\mathcal{T}$ and Φ have positive lengths, and that $0 \in T$, $[0,1] \subseteq \Phi$. If $\zeta(q)$ is linear the process is called mono-fractal, and if $\zeta(q)$ is strictly concave we have a truly multi-fractal process.

A more general definition would be that the limit

$$\zeta(q) = \lim_{\Delta t \to 0} \frac{\log\left[|X(\Delta t)|^q\right]}{\log \Delta t}$$

exists for all q in an open interval $I \subseteq \mathbb{R}$, with $\zeta(q)$ being strictly concave on I.

The structure function is a concave function as shown in equation (2.6). If $q = 0$ we get $\zeta(0) = 0$ regardless of the process at hand.

As long as the moments exists, a self similar process $\{X(t) \mid t \geq 0\}$ with self similarity exponent H, satisfies the relation $X(\Delta t) \stackrel{d}{\sim} \Delta t^H X(1)$ and $E(\mid X(\Delta t) \mid^q) = \Delta t^{Hq} E(\mid X(1) \mid^q)$. Hence

$$\zeta(q) = Hq.$$

In the case of self-similar processes with linear structure function, the scaling behavior is determined by a unique parameter H. The scaling function is then called uniscaling, unifractal or monofractal.

2.5 Construction of the MMAR Model

We start by defining fractional Brownian motion:

Definition 2.2. *Let $H \in (0,1]$. A Gaussian process $\{B_H(t) \mid t \geq 0\}$ is a fractional Brownian motion if*

- $E\left[B_H(t)\right] = 0\ ,\ \ \forall t \geq 0$
- $E\left[B_H(1)^2\right] < +\infty$
- $E\left[B_H(t)\ B_H(s)\right] = \frac{1}{2}\left[t^{2H} + s^{2H} - |t-s|^{2H}\right]\ E[B_H(1)^2]$

If $E\left[B_H(1)^2\right] = 1$ we say that we have a standard fractional Brownian motion. A Brownian motion is a special case of the fractional Brownian motion with $H = 1/2$. It is easy to show that $B_H(t)$ is H-self-similar and has stationary increments.

Let the process $\{\Theta_\mu(t) \mid t \in [0,1]\}$ where $\Theta_\mu(t)(\underline{k}) = \nu_{\underline{k}}([0,t])$ and $\nu = \chi_*\mu$ be as constructed in section 2.1 or 2.1.1. Let $\{B_H(t) \mid t \geq 0\}$ be a fractional Brownian motion defined on a probability space $(\Omega, \mathcal{F}, m)$. We define a stochastic process $\{X_{H,\mu}(t) \mid t \in [0,1]\}$ by:

$$\begin{aligned} X_{H,\mu}(t) &: (\Omega \times \mathcal{T}_N, \mathcal{F} \otimes \mathcal{B}, m \times u) \to \mathbb{R} \\ X_{H,\mu}(t)(\omega, \underline{k}) &= B_H(\Theta_\mu(t)(\underline{k}))(\omega). \end{aligned}$$

The structure function of such a compound process is:

$$S_q(\Delta t) = E_{m\times u}\left[|X_{H,\mu}(\Delta t)(\omega, \underline{k})|^q\right].$$

We find that

$$\begin{aligned} E\left[|X_{H,\mu}(\Delta t)|^q\right] &= \int\limits_{\Omega\times\mathcal{T}_N} |B_H(\Theta_\mu(\Delta t)(\underline{k}))|^q\, d(m\times u) \\ &= \int\limits_{\mathcal{T}_N} \left[\int\limits_{\Omega} |B_H(\Theta_\mu(\Delta t)(\underline{k}))|^q\, dm(\omega)\right] du(\underline{k}) \\ &= \int\limits_{\mathcal{T}_N} c(q)\Theta_\mu(\Delta t)(\underline{k})^{Hq} du\,(\underline{k}) \\ &= c(q)E_u\left[\Theta_\mu(\Delta t)^{Hq}\right]. \end{aligned}$$

The scaling function is then:

$$\begin{aligned} \zeta_{X_{H,\mu}}(q) &= \lim_{\Delta t\to\infty} \frac{\log E\left[|X_{H,\mu}(\Delta t)(\omega, \underline{k})|^q\right]}{\log \Delta t} \\ &= \lim_{\Delta t\to\infty} \frac{\log c(q) + \log E\left[|X_{H,\mu}(\Delta t)(\omega, \underline{k})|^q\right]}{\log \Delta t} \\ &= \zeta_{\Theta_\mu}(Hq). \end{aligned}$$

A theorem given by M. Rypdal [19]:

Theorem 2.1. *Let $\{X(t) \mid 0 \le t \le 1\}$ be a compound process (MMAR-process) generated from a σ-invariant measure $\mu \in \mathcal{M}(\Sigma_2^+)$. Then*

- *$\{X(t)\}$ has stationary increments.*
- $\zeta_{X_{H,\mu}}(q) = 1 + T_{\chi_* \mu}(Hq)$

For a standard Brownian motion $B(t)$ the scaling function is $\zeta_B(q) = 1 + T_\nu(\frac{q}{2})$. In general, knowing that $T_\nu(1) = 0$ we can find the Hurst exponent H as $\zeta_X(\frac{1}{H}) = 1$.

2.6 Structure Functions

Let $\{X(t)|t \ge 0\}$ be a real valued stochastic process. We define the structure functions as:

$$S_q(\Delta t) = E[|X(\Delta t)|^q].$$

If the stochastic process has stationary increments we have:

$$\text{For all } t \ge 0 : S_q(\Delta t) = E[|X(t + \Delta t - X(t)|^q],$$

and if the process is self-similar with exponent H:

$$\begin{aligned}(a > 0) : S_q(a\Delta t) = E[|X_a(\Delta t)|^q] = a^{Hq} E\left[|X(\Delta t)|^q\right] = a^{Hq} S_q(\Delta t) \\ \Rightarrow S_q(\Delta t) = c(q)\Delta t^{Hq}.\end{aligned}$$

We define the scaling function $\zeta(q)$ by the relation

$$S_q(\Delta t) \sim \Delta t^{\zeta(q)} \text{ as } \Delta t \to 0,$$

i.e.

$$\zeta(q) = \lim_{\Delta t \to 0} \frac{\log S_q(\Delta t)}{\log \Delta t}.$$

Using Hölders inequality and letting $t \in (0, 1)$, we get:

$$\begin{aligned}E[|X(\Delta t)|^{tq+(1-t)q'}] = E[(|X(\Delta t)|^q)^t (|X(\Delta t)|^{q'})^{1-t}] \le E[|X(\Delta t)|^q]^t E[|X(\Delta t)|^{q'}]^{1-t} \\ (\text{for } \Delta t < 1) \Rightarrow \lim_{\Delta t \to 0} \frac{\log S_{tq+(1-t)q'}(\Delta t)}{\log \Delta t} \\ \ge \lim_{\Delta t \to 0} t \frac{\log S_q(\Delta t)}{\log \Delta t} + \lim_{\Delta t \to 0} (1-t) \frac{\log S_{q'}(\Delta t)}{\log \Delta t} \\ \Rightarrow \zeta(q) \text{ is a concave function.}\end{aligned}$$

When considering processes defined over unbounded intervals we can only determine multiscaling over bounded intervals. The range of such bounds may be defined on arbitrarily large time intervals. In practice time series are always finite. We may restrict to studying processes on the interval $I = [0, 1]$.

2.7 Structure functions for Measures

Let μ be a Borel measure on Σ_N^+ and $\nu = \chi_* \mu$ be the induced measure on the interval I with respect to the map χ constructed in section 2.1. Define the structure function of ν as

$$S_q(\Delta t) = \sum_{i_1,\ldots,i_n} \mu([i_1 \ldots i_n])^q.$$

The scaling function is assumed to satisfy the relation: $S_q(\Delta t) \sim \Delta t^{T_\nu(q)}$. In a more general setting the scaling function of the measure is:

$$T_\nu(q) = \lim_{\epsilon \to 0} \frac{\log \inf_{\mathcal{U}_\epsilon} \sum_{U \in \mathcal{U}_\epsilon}, \nu(U)^q}{\log \epsilon},$$

where infimum is taken over all ϵ-covers of $\mathcal{U}_\epsilon$ of I. For a random measure $\nu_{\underline{k}} = \chi_* \mu_{\underline{k}}$ as constructed in section 2.1 (section 2.1.1) we have:

$$T_{\nu_{\underline{k}}}(q) = T_\nu(q) = \lim_{n \to \infty} \frac{\log \sum_{i_1 \ldots i_n} \mu([i_1 \ldots i_n])^q}{\log \Delta t}.$$

If μ is a Bernoulli-measure we have

$$T_{\nu_{\underline{k}}}(q) = \lim_{n \to \infty} \frac{\log \sum_{i_1 \ldots i_n} (p_{i_1}^q \cdots p_{i_n}^q)^n}{-n \log N} = \lim_{n \to \infty} \frac{\log (p_1^q + \ldots + p_N^q)^n}{-n \log N} = -\frac{\log (p_1^q + \ldots + p_N^q)}{\log N},$$

where $\Delta t = N^{-n}$.

2.7.1 Markov Measures

If μ is a Markov measure with transition matrix π, then

$$T_\nu(q) = -\frac{\log \rho(\|\pi_{ij}^q\|)}{\log N} \tag{2.8}$$

where $\Delta t = N^{-n}$ and ρ denotes the spectral radius. Function 2.8 is a special case of Bowen's equation [16].

3 Analysis of the Auroral Electrojet Index

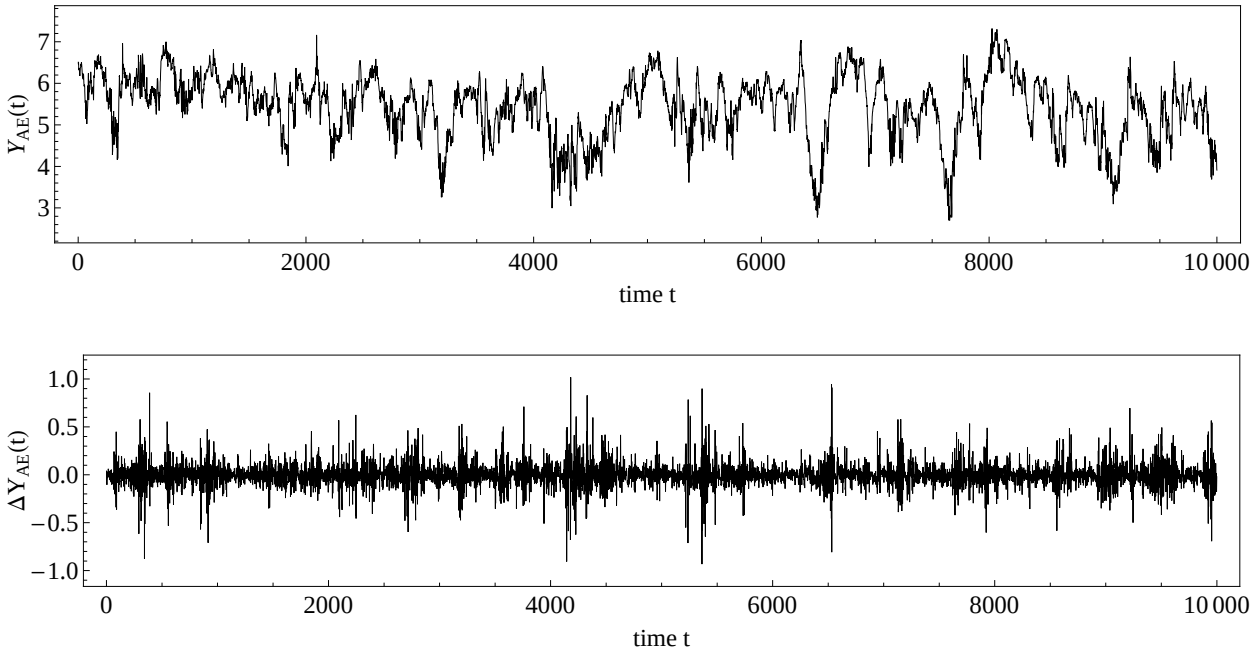

Figure 3.1: The logarithmic AE Index and its increments.

Let $X_{\text{AE}}(t)$ denote the AE Index. We will study the time series $Y_{\text{AE}}(t) = \log X_{\text{AE}}(t)$. We take the logarithm in order to make the data better suited for modeling with stochastic processes with stationary increments. This is the same transformation that is (always) applied to financial price data. In fact, for positive time series, such as financial data or the AE Index, there is often a relationship between the amplitude of the increment at time t and the value of the signal at time t. Such a relationship is inconsistent with stationary increments. however, this effect (more of less) vanishes after we have taken the logarithm of the signal. A segment of $Y_{\text{AE}}(t)$ is shown in figure 3.1. In total we consider 3 156 480 data points of the AE Index over the years 2000 to 2005. We will try to extract some robust structures that can characterize the underlying physical processes in the formation of the AE currents.

In figure 3.2(a) we have shown the structure functions of the AE Index with q from 1 to 7, and over time scales from 2^1 to 2^8. We have taken log-log values of the structure functions to make linear comparisons. The scaling function as shown in figure 3.2(b) suggest multi-fractal behavior. The dotted intersection at $\zeta(\frac{1}{H}) = 1$ indicate the Hurst exponent of the outer process at about 0.41.

The process $|Y_{AE}(t+1) - Y_{AE}|^{\frac{1}{H}}$ can be seen as an approximation to the underlying measure with distribution function $\Theta(t)$. In figure 3.3 we have estimated the structure functions of this extracted measure. The scaling function of the measure $T_\nu(q)$ almost overlaps the the

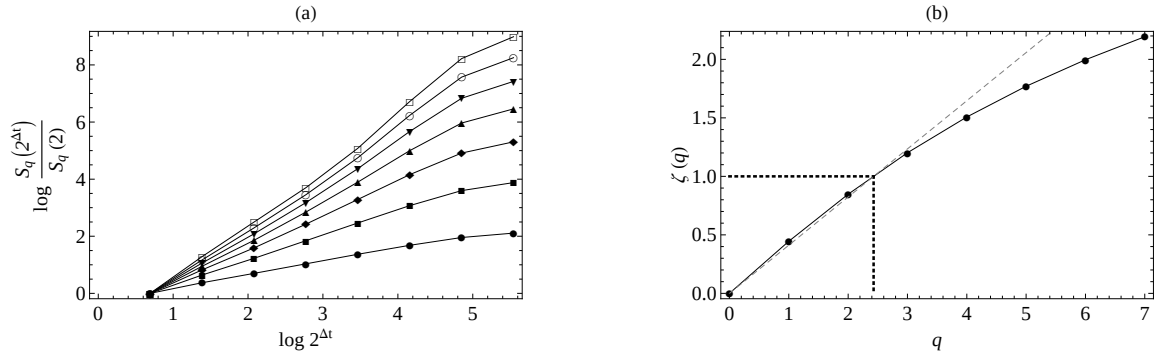

Figure 3.2: (a): The structure functions of the AE Index for values of q from 1 to 7, and time scales from 2^1 to 2^8. (b): The estimated scaling function (least squares method). The dotted intersection at $\zeta(\frac{1}{H}) = 1$ indicate the estimated Hurst exponent $H = 0.41$. The continuous concave curve is the computed scaling function of the AE Index.

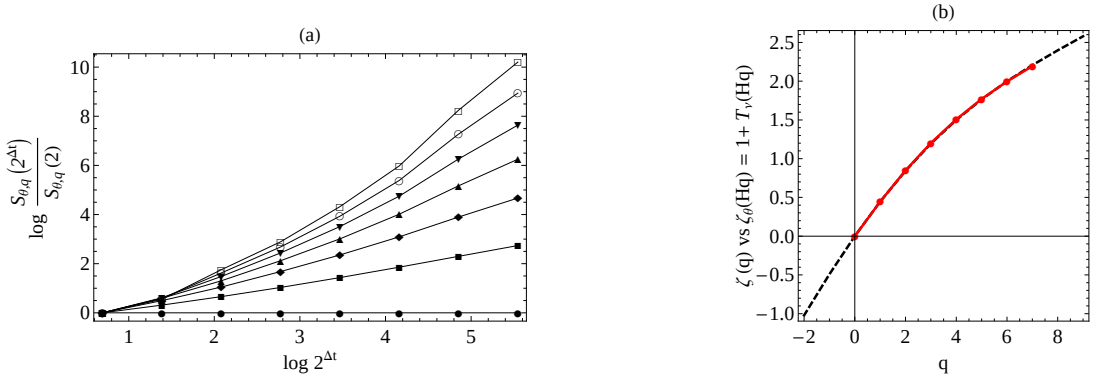

Figure 3.3: (a): The structure functions of the extracted measure of the AE Index. (b): The theoretical scaling function (represented as the dashed curve) from the relation $\zeta(q) = 1 + T_\nu(Hq)$. The continuous curve (that overlaps the dashed curve) is the scaling function found from the AE Index, for values of q between 1 and 7.

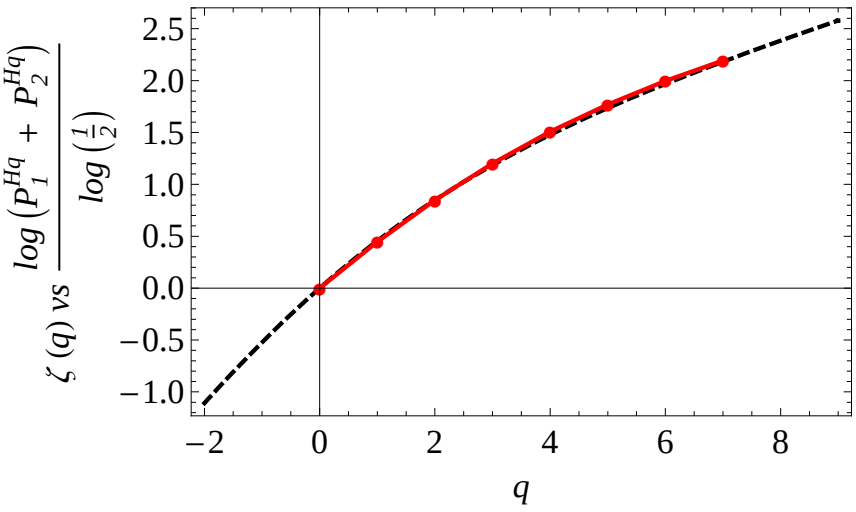

Figure 3.4: Scaling function of the AE Index compared with the theoretical scaling function of a Bernoulli measure with with probabilities P_1 and P_2. The best fit reveals $P_1 = 0.26$ and $P_2 = 1 - P_1$.

scaling function of the AE Index when we apply the relation $\zeta_X(q) = 1 + T_\nu(Hq)$.

For a Bernoulli measure with probabilities $P = \{P_1, P_2\}$, where $P_1 + P_2 = 1$, the corresponding theoretical scaling function is $\zeta(q) = -\frac{\log(P_1^q + P_2^q)}{\log 2}$. The probabilities that best fit the scaling function of the AE Index were found to be $P_1 = 0.26$ and $P_2 = 1 - P_1$, as seen in figure 3.4.

The observed multi-fractality gives reasons to discuss the dimension function D_q as given by i.a. Feder 1989 [9]. The spectrum of fractal dimensions D_q for the AE Index is shown in figure 3.5. A monofractal measure would give constant D_q. For Bernoulli measures D_q equals the Hentchel-Procaccia dimension spectrum defined earlier. The multi-fractal spectrum of the AE Index is shown in figure 3.6 where α is the pointwise dimensions of the extracted measure.

3.1 Probability Density Functions

In the MMAR model the probability density function(s) (pdf) $P_{X,t}(x)$, of $X(t)$, are

$$P_{X,t}(x) = \int (P_{B,s}(x)\ P_{\theta,t}(s))ds, \tag{3.1}$$

where we recall that $B_H(t)$ and $\theta(t)$ are independent.

We know that $B_H(t)$ is H-self similar:

$$B_H(at) \stackrel{d}{=} a^H B(t) \text{ for all } a > 0.$$

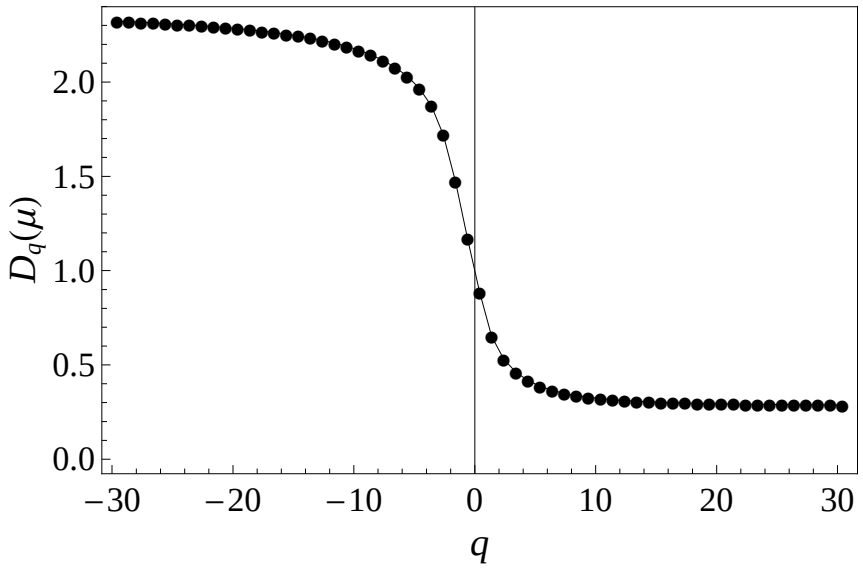

Figure 3.5: D_q is the spectrum of fractal dimensions for the extracted measure. Here we found the fractal dimension spectrum of the AE Index.

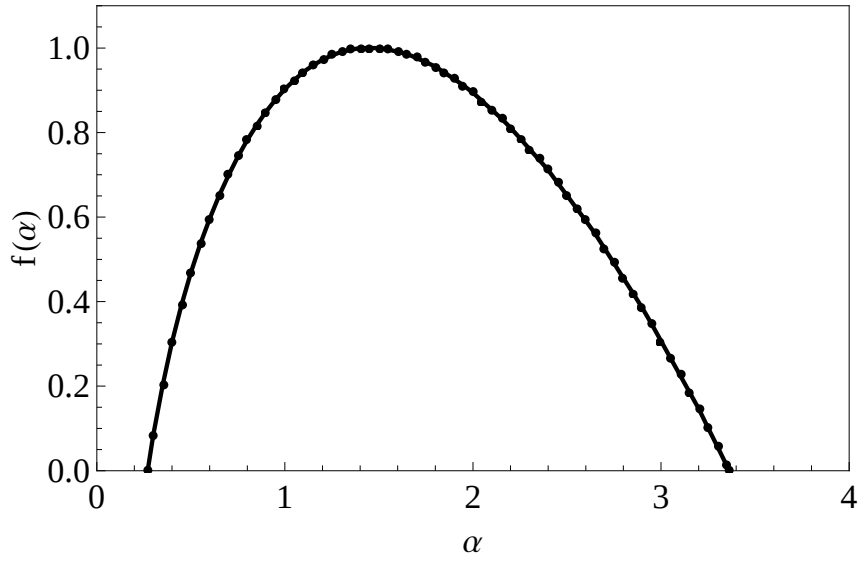

Figure 3.6: The multi-fractal spectrum of the AE Index calculated from the extracted measure via the Legendre transform.

Substituting $x = az$ where $\frac{dz}{dx} = \frac{1}{a}$ and $z = \frac{x}{a}$ we get

$$\begin{aligned} P_B(x) &= P_Z(z)\frac{dz}{dx} \\ &= P_Z\left(\frac{x}{a}\right)\frac{1}{a} \\ &\Downarrow \\ P_{B,at}(x) &= \frac{1}{a^H}P_{B,t}\left(\frac{x}{a^H}\right). \end{aligned}$$

Hence $P_{B,t}(0) \sim t^{-H}$.

By definition of fractional Brownian motion we have expectation

$$E\left[B_H(\Delta t)\right] = 0$$

for all $\Delta t \geq 0$, and

$$B_{H,s}(x) \sim N(0, \sigma_B(s)).$$

The variance $\mathrm{Var}(B_H(\Delta t))$ satisfies the relation $\mathrm{Var}(B_H(\Delta t)) = E\left[B_H^2(\Delta t)\right] = \Delta t^{2H}$. Thus $\sigma_B = s^H$, where H is the Hurst exponent. The pdf of $B_H(t)$ is then

$$P_{B,s}(x) = \frac{1}{\sqrt{2\pi s^{2H}}}\exp\left(-\frac{x^2}{2s^{2H}}\right),$$

where the peak scales as $P_{B,s}(0) = \frac{1}{\sqrt{2\pi}}s^{-H} \sim s^{-H}$.

Considering the probability density function in equation 3.1 we can find the scaling of the peaks of $P_{X,t}$ as:

$$\begin{aligned} P_{X,t}(0) &= \frac{1}{\sqrt{2\pi}}\int \left(s^{-H}\ P_{\theta,t}(s)\right) ds \\ &= \frac{1}{\sqrt{2\pi}}E\left[\theta(t)^{-H}\right] \\ &\sim t^{\zeta_\theta(-H)} = t^{\zeta_X(-1)}. \end{aligned} \tag{3.2}$$

We note that $\zeta_X(-1)$ may not exist. However, we can just extend the definition of $\zeta_X(q)$ to all $q \in \mathbb{R}$ through the formula

$$\zeta_X(q) = \zeta_\Theta(Hq).$$

Let the scaling exponent ν be defined by $P_{X,\Delta t}(0) \sim \Delta t^{-\nu}$.

Then $\zeta_X(-1) = -\nu$. In the AE dataset we found ν to be approximately 0.52. This is found from estimations of peaks of pdf, see figure 3.7. We can check this result in figures 3.3(b) and 3.4. Observing that $H \neq \nu$ indicate multi-fractal behavior, supporting a curvature of the scaling function. A monofractal process would yield equality of the scaling parameters, i.e. $H = \nu$.

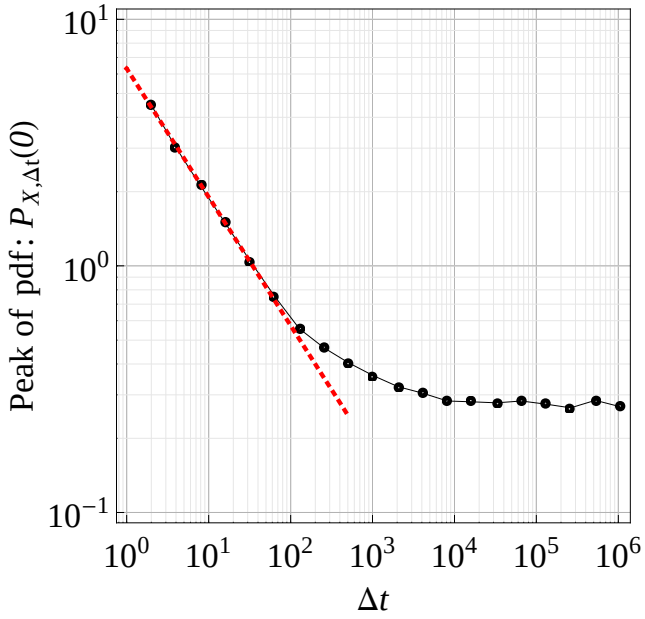

Figure 3.7: Estimating ν by the scaling of the peaks of $P_{X,t}$. We found ν to be approximately 0.52.

3.2 Log-normal Multiplicative Cascades

Let $\Theta(t) = m([0,t])$ where m is a random multi-fractal measure on $I = [0,1]$. The measure can be constructed as a b-adic multiplicative cascade. A b-adic interval is

$$\Delta_{i_1,\ldots,i_n} = \left[(0.i_1 i_2 \ldots i_n)_b, (0, i_1 i_2 \ldots i_n)_b + \frac{1}{b^n}\right].$$

The measure of a b-adic interval is defined as

$$m(\Delta_{i_1,\ldots,i_n}) = \omega_{i_1}\omega_{i_1 i_2}\ldots\omega_{i_1,\ldots,i_n} M_{i_1,\ldots,i_n},$$

where ω_i are independent, identically distributed, non-negative random variables and

$$M_{i_1,\ldots,i_n} = \lim_{k\to+\infty} \sum_{j_1,\ldots,j_k} \omega_{i_1\ldots i_n j_1}\omega_{i_1\ldots i_n j_1 j_2}\cdots\omega_{i_1\ldots i_n j_1\ldots j_k}.$$

as defined by Mandelbrot, Fisher and Calvet 1997 [15].

We assume $E[\omega] = \frac{1}{b}$, thus on an average conserving the mass at each step in the construction. We choose to let ω have a log-normal distribution with parameters μ and σ. For this distribution the relations for the mean and variance are (i.a. Edwin and Kunio [7]):

$$E[\omega] = \frac{1}{b} = \exp\left(\mu + \frac{1}{2}\sigma^2\right)$$
$$\mu = -\frac{1}{2}\sigma^2 - \log(b).$$

At construction level $n \in \mathbb{N}$:

$$\begin{aligned} E\left[\prod_{k\leq n}\omega_{i_1\ldots i_k}\right] = n\mu &= -\frac{\log\Delta t}{\log b}\left(-\frac{1}{2}\sigma^2 - \log(b)\right) \\ &= \frac{\sigma^2}{2\log b}\log\Delta t + \log\Delta t \\ &= (1+\lambda)\log\Delta t \end{aligned}$$

where $\lambda = \frac{\sigma^2}{2\log b}$ and σ is the standard deviation of $\log\omega$, and $\Delta t = b^{-n}$. We have

$$\begin{aligned} \mathrm{Var}\left(\prod_{k\leq n}\omega_{i_1\ldots i_k}\right) &= \left(\exp\left(\sigma^2\right) - 1\right)\exp\left(2\mu + \sigma^2\right) = n\sigma^2 \\ &= -\frac{\log\Delta t}{\log b}\sigma^2 = -2\lambda\log\Delta t. \end{aligned}$$

The distribution of this product is the log-normal with pdf

$$P_{\theta,\Delta t}(x) = \frac{1}{x\sqrt{-4\pi\lambda\log\Delta t}}\exp\left(-\frac{(\log x - (1+\lambda)\log\Delta t)^2}{-4\lambda\log\Delta t}\right). \tag{3.3}$$

We then have an expression of the probability density function of the process $X(t)$:

$$\begin{aligned} P_{X,\Delta t}(x) &= \int_0^{+\infty}\left(P_{B_s}(x)\ P_{\theta,\Delta t}(s)\right)ds \\ &= \int_0^{+\infty}\frac{1}{\sqrt{2\pi s^{2H}}}\exp\left(-\frac{x^2}{2s^{2H}}\right)P_{\theta,\Delta t}(s)ds, \end{aligned} \tag{3.4}$$

where $P_{\theta,\Delta t}(s)$ is given by equation 3.3.

By Mandelbrot, Fisher and Calvet [15] we known that the scaling function of the time process is $\zeta_\theta(q) = \log_b E\left[\omega^q\right]$. It follows that $\zeta_X(q) = \zeta_\theta(Hq) = \log_b E\left[\omega^{Hq}\right]$:

$$\begin{aligned} E\left[\theta(\Delta t)^{Hq}\right] &= \int_0^{+\infty} s^{Hq}P_\theta(s)ds \\ &= \int_0^{+\infty}\frac{s^{Hq-1}}{\sqrt{-4\pi\lambda\log\Delta t}}\exp\left(-\frac{(\log s - (1+\lambda)\log\Delta t)^2}{-4\lambda\log\Delta t}\right)ds \\ &\sim \Delta t^{Hq(1+\lambda-Hq\lambda)} \\ &\Downarrow \\ \zeta_X(q) &= (1+\lambda)Hq - \lambda(Hq)^2. \end{aligned} \tag{3.5}$$

From the AE Index we found the Hurst exponent to be $H = 0.41$ through the relation $\zeta_X(\frac{1}{H}) = 1$. Solving the scaling function in equation 3.5 knowing $\zeta_X(-1) = -\nu$ we get:

$$\lambda = \frac{\nu - H}{H(1+H)} \approx 0.19.$$

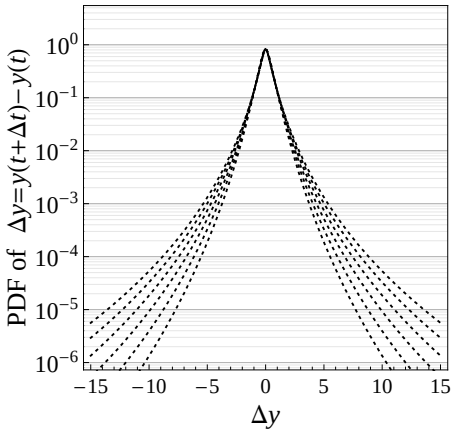

Figure 3.8: Pdfs of $P_{\Upsilon,\Delta t}$ with the parameters estimated from the AE Index: $H = 0.41$, $\nu = 0.52$ and $\lambda = 0.19$.

A plot of the pdfs of $Y_{\text{AE}}(t+\Delta t) - Y_{\text{AE}}(t)$ using the estimated parameters found from the AE Index is shown i figure 3.8.

Better results are found in the case where $\Theta(t)$ is induced by a random Bernoulli-measure. As previous we choose time increment $\Delta t = 2^{-n}$. The scaling function of the process $X(t)$ becomes:

$$\zeta_X(q) = 1 - \frac{\log\left(P_1^{Hq} + P_2^{Hq}\right)}{\log 2},$$

and for the AE data set we found Hurst exponent $H = 0.41$ and $\nu = 0.52$. Using the relation $\zeta_X(-1) = -\nu$, the probabilities are:

$$P_1^{-H} - P_2^{-H} = 2^{\nu+1}$$
$$\Downarrow$$
$$P_1 = 0.26 \text{ and } P_2 = 1 - P_1.$$

Using equation 3.4 we find the probability density function to $X(t+\Delta t) - X(t)$ when the time process is the distribution function of a random Bernoulli measure. Remembering that the time process is defined as $\Theta_\mu(t)(\underline{k}) = (\chi_* \mu_{\underline{k}})([0,t])$, the mass of $\Delta_{i_1,\ldots,i_n}$ is a product on the form $s = P_{i_1} \cdots P_{i_n} = P_1^k \; P_2^{n-k}$. Suppose that we have n independent trials, each with probability P_1 of "success" and P_2 of "failure". The number of successes that occur in the n trials are then said to be binomial random distributed with parameters (n, p) (i.a. Ross [18]). For $\Delta t = 2^{-n}$ the probability density function of the increment $\Theta(t+\Delta t) - \Theta(t)$ is then:

$$P_{\theta,\Delta t}(s) = \frac{1}{2^n} \sum_{k=0}^{n} \binom{n}{k} \delta(s - P_1^{Hk} \; P_2^{H(n-k)}),$$

where δ is the delta function. Applying to the equation 3.4 gives the probability density function of the process $X(t)$:

$$P_{X,\Delta t}(x) = \frac{1}{\sqrt{2\pi}2^n} \sum_{k=0}^{n} \binom{n}{k} P_1^{Hk}\ P_2^{H(n-k)} \exp\left(-\frac{x^2}{2P_1^{2Hk} P_2^{2H(n-k)}}\right). \tag{3.6}$$

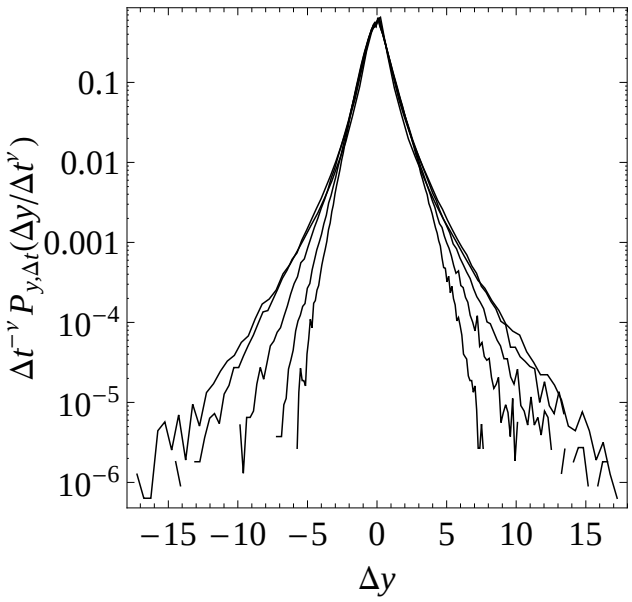

Figure 3.9: The probability density functions of $Y_{\text{AE}}(t + \Delta t) - Y_{\text{AE}}(t)$ for $\Delta t = 2^0, ..., 2^6$.

In figure 3.10 we model the pdfs for the AE Index using the probabilities and parameters, $P_1 = 0.26$, $H = 0.41$, and $\nu = 0.52$. Replacing the parameters in equation 3.6 we find appropriate theoretical distributions for the AE dataset.

In figure 3.11 we notice an agreement with overlapping spreading of tails in the pdfs for varying Δt in the AE Index compared with the constructed model (represented as dashed curves). In the AE dataset we estimate distributions for time scales from 2^0 to 2^6. Best estimates are found with the time scales from 2^{-6} to 2^{-11} in the model.

In figure 3.12 we have compared the AE Index with a Brownian motion which scales as a monofractal. This gives collapsing and overlapping probability density functions, with shapes that are independent of time scale Δt.

Takalo *et al.* [22] used fractional Brownian motion as a model of the auroral indices. Some discuss the use of truncated Lévy motions i.a. Kabin and Papitashvili 1998 [12] suggesting a closer relation to Lévy flights representing the interplanetary magnetic field; Consolini *et al.* 1997 [6] mention that magnetic field fluctuations in the polar cap seem to be compatible with truncated Lévy flight processes; Hnat *et al.* 2002 [11] stating that the pdf of the velocity and magnetic field fluctuations are well described by the Gamma distribution arising from a finite range Lévy walk; Bruno *et al.* 2004 [4] find pdfs resembling Lévy flight behavior of interplanetary solar-wind fluctuations in the inner heliosphere. Fractional Lévy motion has been applied representing AE Index among other space plasma physics time series, in Watkins [23]. The AE dataset has a scaling function which arguably flattens out near 1 for

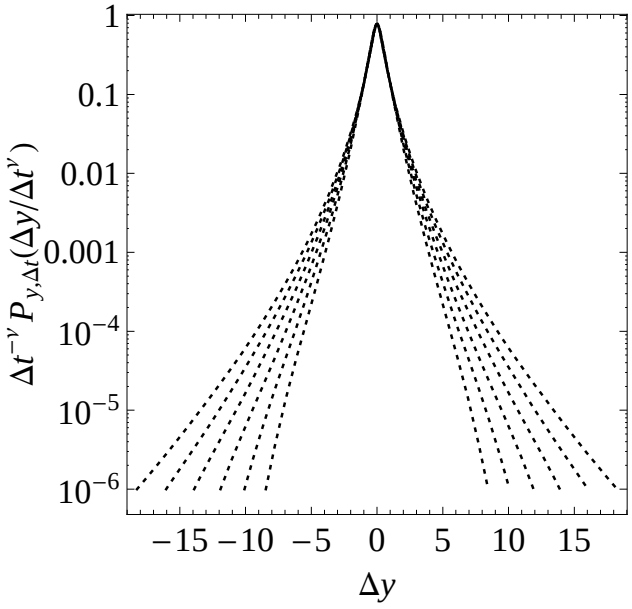

Figure 3.10: Modeling of pdfs for the AE Index. The modeling process is a compound fractional Brownian motion with the distribution function of a Bernoulli measure. The probabilities and parameters are those related to the AE Index i.e. $P_1 = 0.26$, $P_2 = 1 - P_1$, $H = 0.41$, and $\nu = 0.52$.

higher values of q. This does not require a multiplicative process to explain such property. The concave behavior can be understood as a bifractality of the truncated fractional Lévy motion. Due to numerical estimations a curved break around 1 is expected.

As is seen in figure 3.14 there is little support of the AE Index being a monofractal random process. Certainly Lévy motions have non-Gaussian distributions, but they are self-similar and the pdfs should collapse upon each other under re-scaling with respect to the exponent ν.

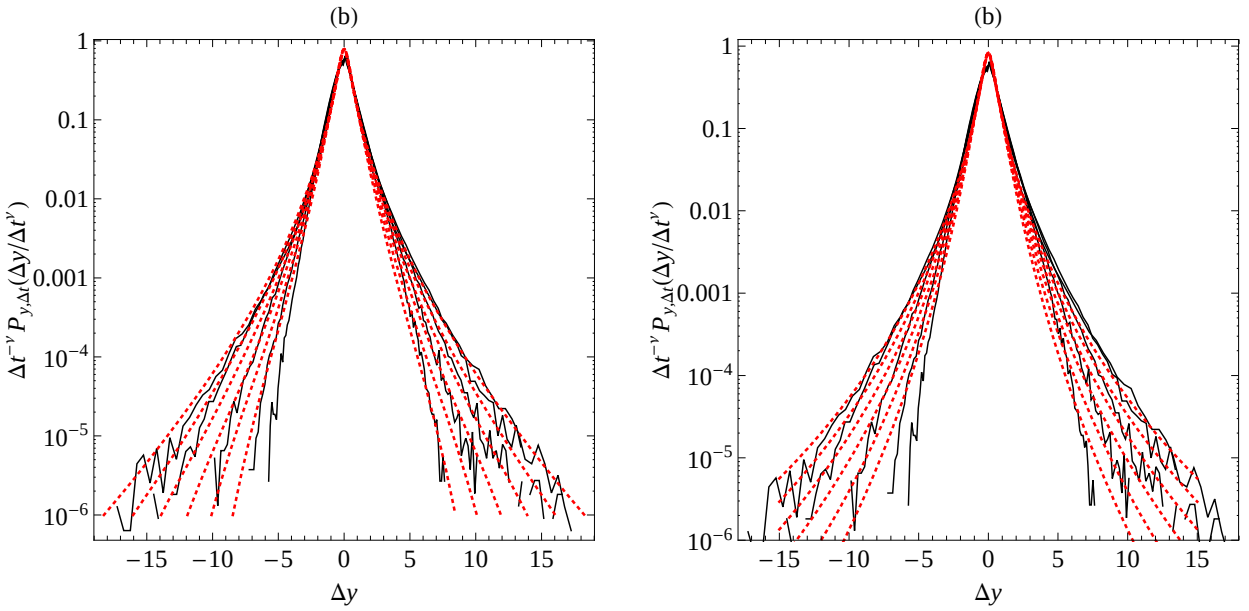

Figure 3.11: (a): Comparing the pdfs of the AE Index with the constructed model with distribution function of a Bernoulli measure, in figure 3.10. The pdfs of AE Index are represented as the continuous curves. The estimated pdfs are represented as the dashed curves. (b): Comparisons with the pdfs in figure 3.8.

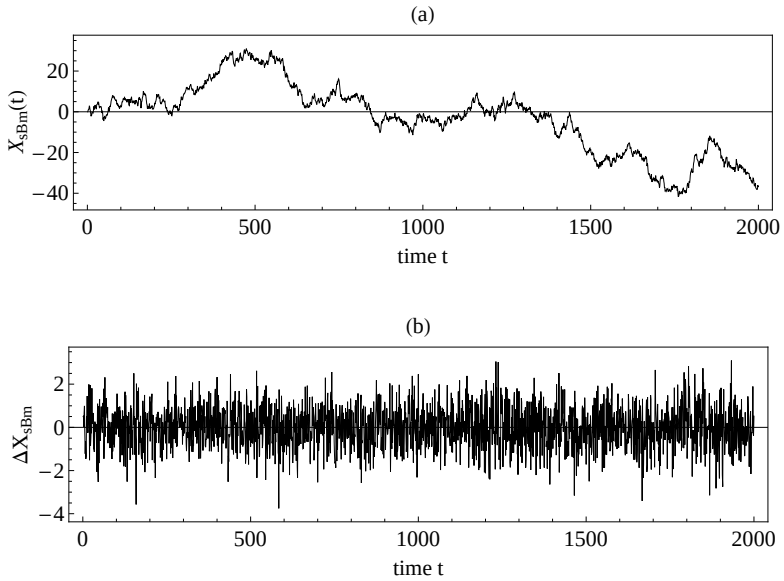

Figure 3.12: (a): Realization of a Brownian motion. (b): The corresponding increments.

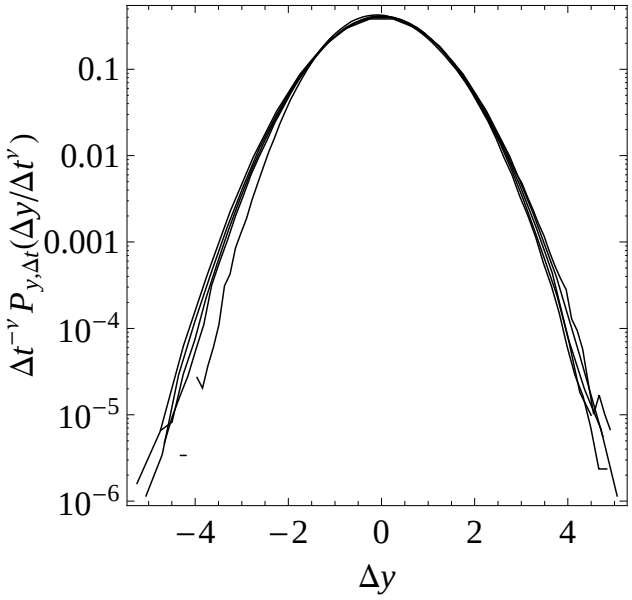

Figure 3.13: Re-scaled pdfs of $Y(t + \Delta t) - Y(t)$ where $Y(t)$ is a Brownian motion.

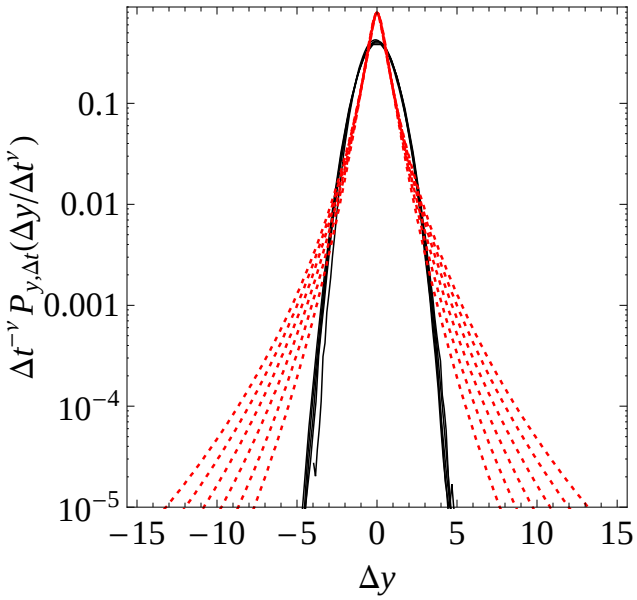

Figure 3.14: Comparing pdfs of a Brownian motion with the pdfs constructed from the AE Index. The pdfs of the Brownian motion are represented as the continuous curves. The estimated pdfs, of the AE Index, are represented as the dashed curves.

4 Conclusion

We have analysed the AE Index over the years 2000 to 2005, and in total of over 3 000 000 data points. Using MMAR-models we have constructed scaling functions of different processes which we have compared with scaling function of the AE Index. Through testing of the scaling functions, determination of fractal dimensions, and considering the shape of the pdfs we have been able to classify multi-fractal properties of the AE Index.

We have applied a compound stochastic process with a random Bernoulli measure. The parameters of the measure were estimated to $P_1 = 0.26$, $P_2 = 0.74$. The Hurst exponent was estimated by $\zeta(\frac{1}{H}) = 1$, and ν which is defined by $\zeta(-1) = -\nu$. In the AE Index we found ν to be approximately $\nu = 0.52$. The Hurst exponent of the AE Index was estimated to be 0.41. Observing that $\nu \neq H$ is an indication of multifractality. The MMAR-model seems to describe the fluctuations in the AE Index well.

Additionally, we have studied probability density functions (pdf) at different time scales Finding exact expressions of the pdfs, using the parameters estimated from the AE Index, produced results comparable with the numerical pdf of the AE Index. We discovered non-Gaussian distribution and spreading of tails for varying time scales in the AE Index, demonstrating deviation from self-similarity. These are characteristics related to multifractality.

Finally we have tested our diagnostic tools on simulated MMAR models. These experiments show that the methods are capable of detecting multifractality, related to the calculation of scaling functions. The results are good if we average over several independent realizations. More details of these findings are in the following chapter.

5 Testing of Methods on Synthetic Data

In this section we simulate various processes in order to test our diagnostic methods.

5.1 Brownian Motion

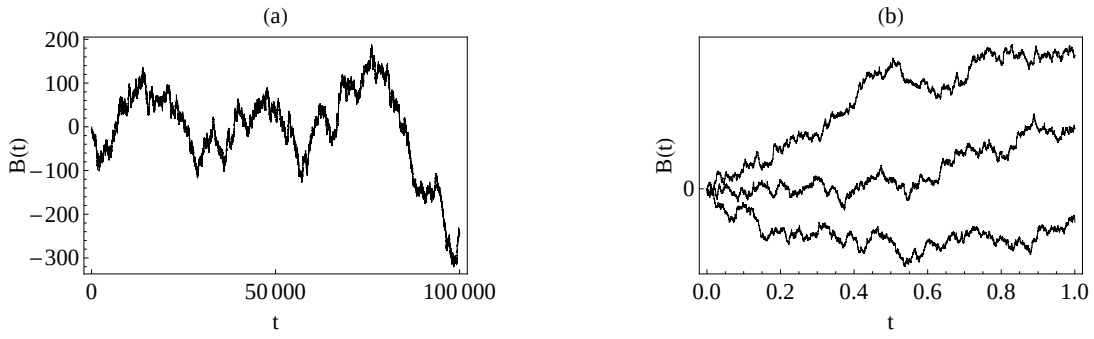

Figure 5.1: (a): Realization of a Brownian motion. (b): Several realizations of a Brownian motion.

In figure 5.1 we have shown realizations of a Brownian motion. A Brownian motion have self similarity exponent $H = 1/2$. We will mainly use Brownian motion, rather than fractional Brownian motion, as a model of the "outer" process, since the accuracy of our methods appear to be better for $H \approx 0.5$.

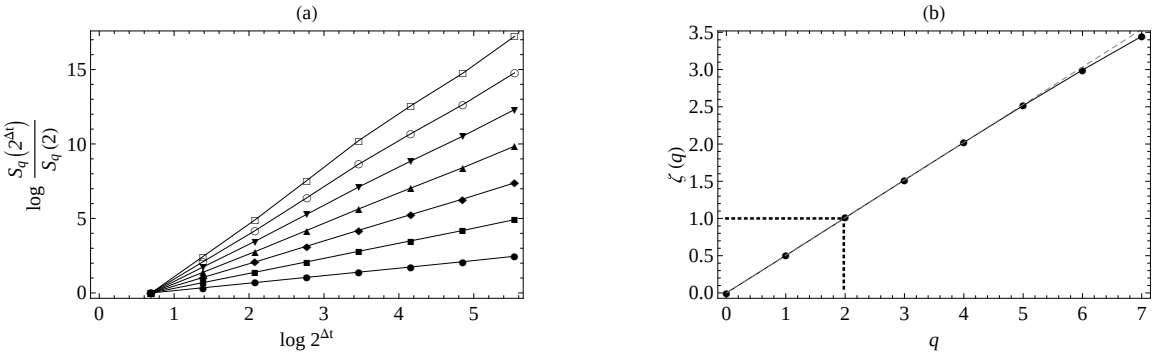

Figure 5.2: (a): Structure functions of a Brownian motion for $q = 1, 2, ..., 8$. The process is simulated with 10^5 data points. (b): Calculated scaling function using least squares method.

In figure 5.2 (a) we show the structure functions $S_q(\Delta t) = E\left[|B(\Delta t)|^q\right]$ of a Brownian motion for integer $q = 1, 2, ..., 8$. We find the linear approximation, using least squares method, from the structure functions. In figure 5.2(b) we show a good linear fit to the

scaling function $\zeta(q) = Hq$, with $H = 0.49$. This is in accordance with the theoretical Hurst exponent $H = 1/2$. This diagnostic tool seems to work well on monofractal processes.

5.2 Multi-fractal Processes

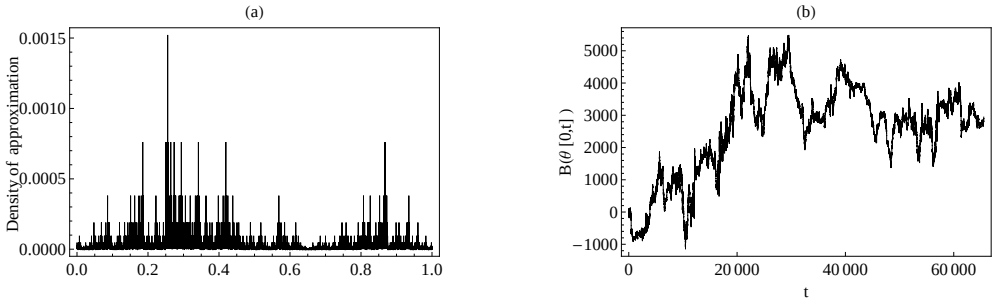

Figure 5.3: (a): Density of an approximation to a random measure. Here we have constructed a Bernoulli measure μ as introduced in section 2.1. (b): A multi-fractal process where the time process $\Theta(t)$ is based on a Bernoulli measure.

In figure 5.3(a) a random Bernoulli measure is constructed from an iterative procedure as introduced in section 2.1. In figure 5.3(b) we show a realization of the compound multi-fractal process. Visually it can be hard to distinguish from a monofractal realization. If the Hurst exponent H of a multi-fractal realization is the same as of a monofractal sample, then the multi-fractal realization will tend to be more jagged and fluctuating in its appearance. This is however not reliable evidence of multi-fractality.

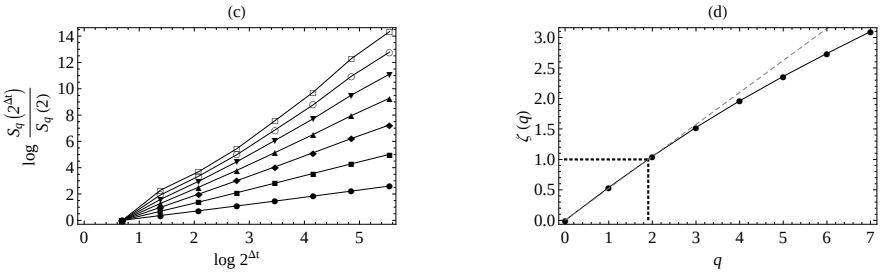

Figure 5.4: (a): Structure functions of a simulated multi-fractal process. (b): The corresponding scaling function. From $\zeta(\frac{1}{H}) = 1$ we find $H = 0.51$.

In figure 5.4 the structure functions and scaling function are computed from a Brownian motion composed with the distribution function of a random Bernoulli measure. The empirical Hurst exponent was found to be 0.51 which is close to the actual Hurst exponent, $H = 1/2$. The dotted line represents a linear function with slope Hq as would be the case

of a monofractal process. The concave scaling function confirms the multi-fractal behavior, as expected.

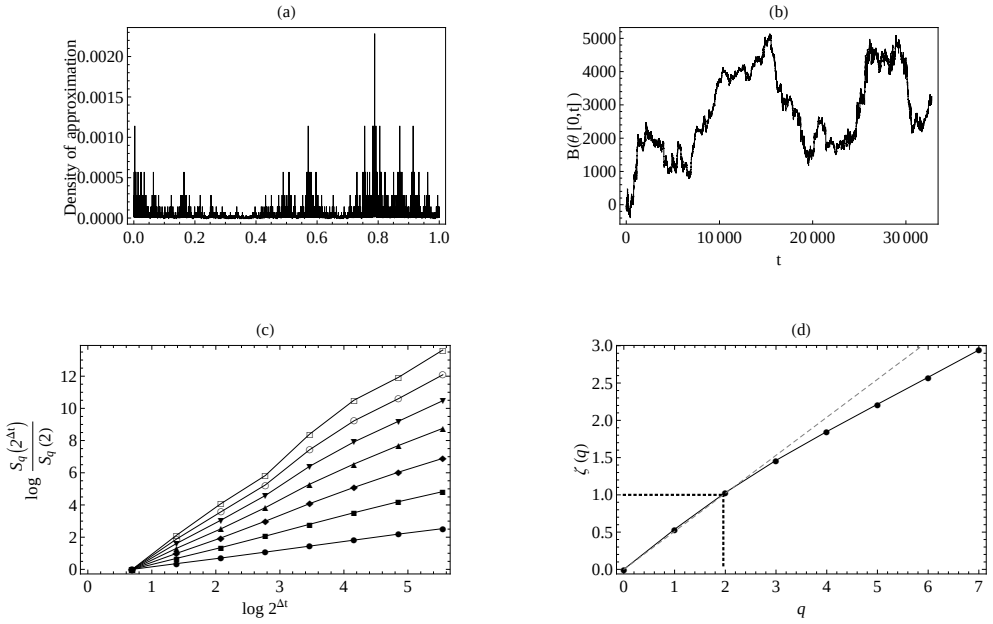

Figure 5.5: (a): Density of approximation to the random Bernoulli measure. (b): Realization of the MMAR-process with Hurst exponent $H = 1/2$. (c): Structure functions of the MMAR-process for $q = 1, ..., 7$ and time scales from 2^1 to 2^8. (d): Scaling function of the MMAR-process calculated using least squares method The Hurst exponent is found to be 0.50.

Making use of the estimated Hurst exponent we compute $|X(t + \Delta t) - X(t)|^{\frac{1}{H}}$ where $X(t) = B(\Theta(t))$. This is an approximation to the measure "hidden" in the MMAR-process.

By construction we have defined a specific measure for this MMAR-process realization. We have the possibility to compare the actual measure and the extracted measure, as shown in figure 5.6. By comparison we see clear similarities.

In figure 5.7 we see reasonable similarities between the distribution functions of the (continuous curve) measure and (dashed) the extracted measure. We have made normalization of the extracted measure on the unit interval.

The scaling function of the realization of the MMAR-process $\zeta(q)$ can be compared with the scaling function of $\zeta_\Theta(Hq) = 1 + T_\nu(Hq)$ where $T_\nu(Hq)$ is the scaling function of the extracted measure. We see reasonable overlapping curves in figure 5.8(a). The scaling function computed in 5.5(d) is represented as the bounded continuous curve. The theoretical scaling function from relation $\zeta_X(q) = 1 + \zeta_\nu(Hq)$ is represented as the dashed line. We find almost identical results when using the exact expression of the Bernoulli measure, where the scaling function of the measure is: $T_\nu(q) = -\frac{\log(P_1^q + P_2^q)}{2}$. This is seen i figure 5.8(b).

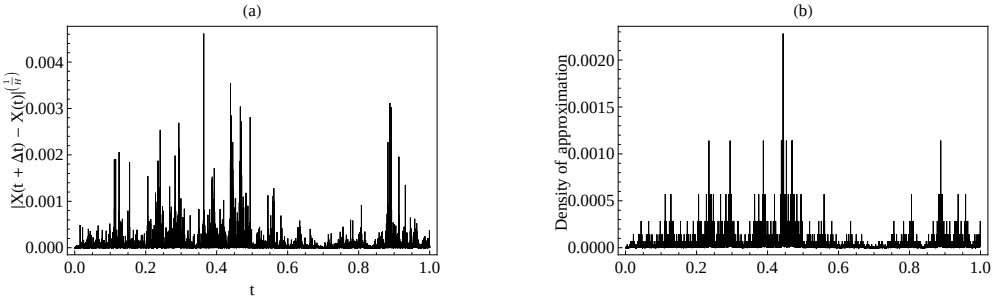

Figure 5.6: Comparing the extracted measure of the realization and the constructed measure for this realization. (a): The extracted measure (b): The actual measure used in the construction of the process.

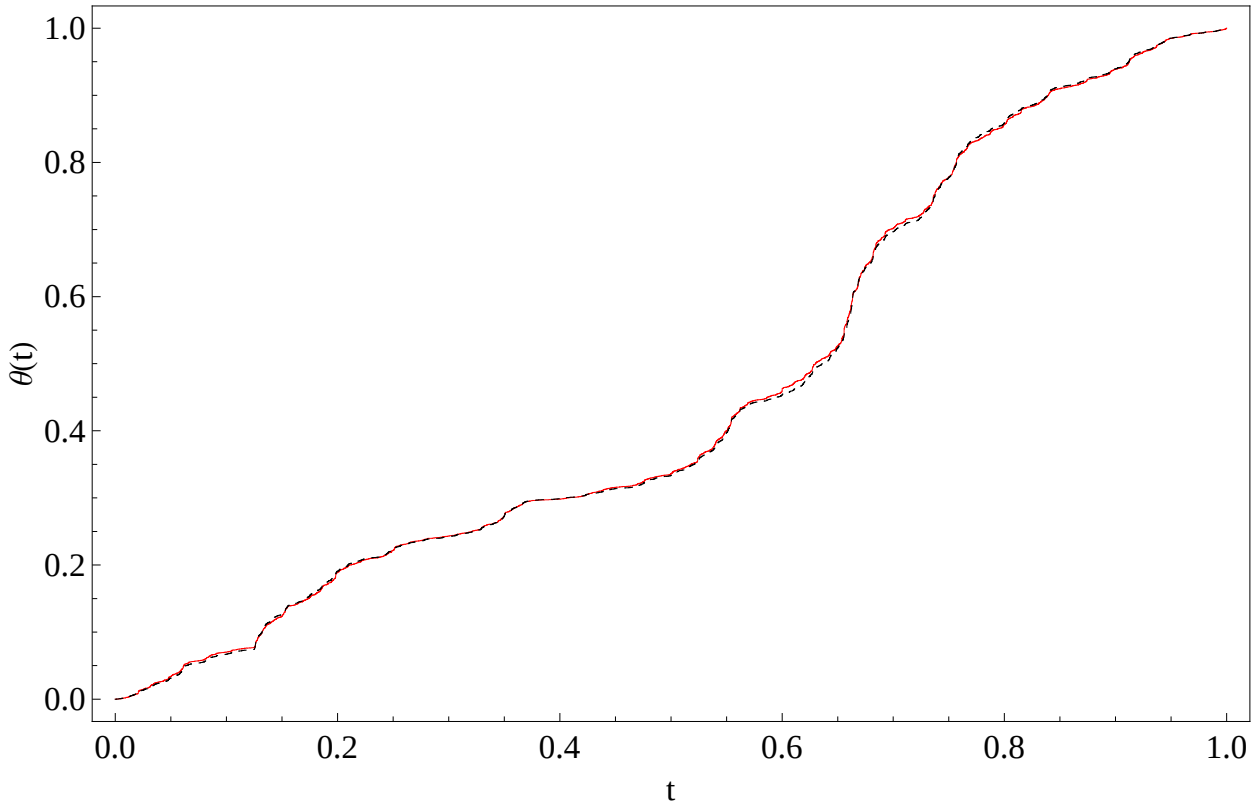

Figure 5.7: The continuous curve represents the distribution function of the measure. The dashed curve is the extracted $\Theta(t)$ of the MMAR-process.

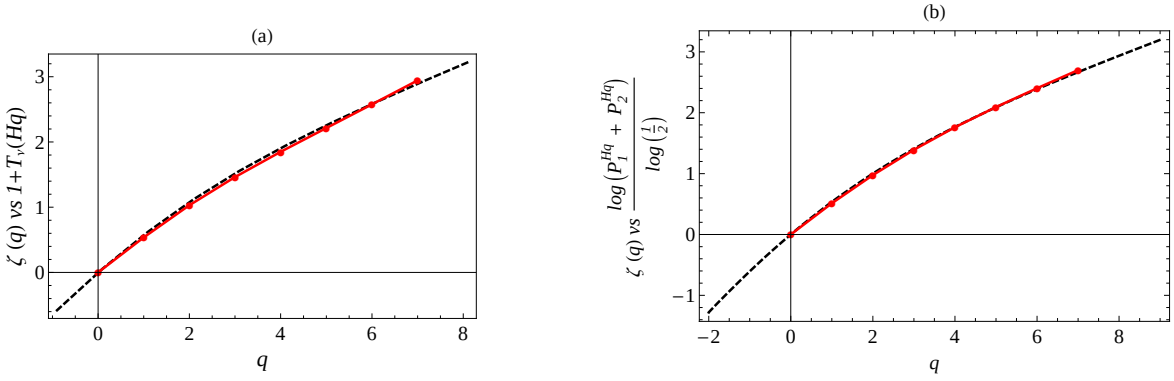

Figure 5.8: (a): The scaling function computed in 5.5(d) is represented as the solid curve. The theoretical scaling function from relation $\zeta_X(q) = 1 + T_\nu(Hq)$ is represented as the dashed curve. (b): The exact expression of the scaling function of a Bernoulli measure as the dashed curve. It is compared with the estimated scaling function in 5.5(d).

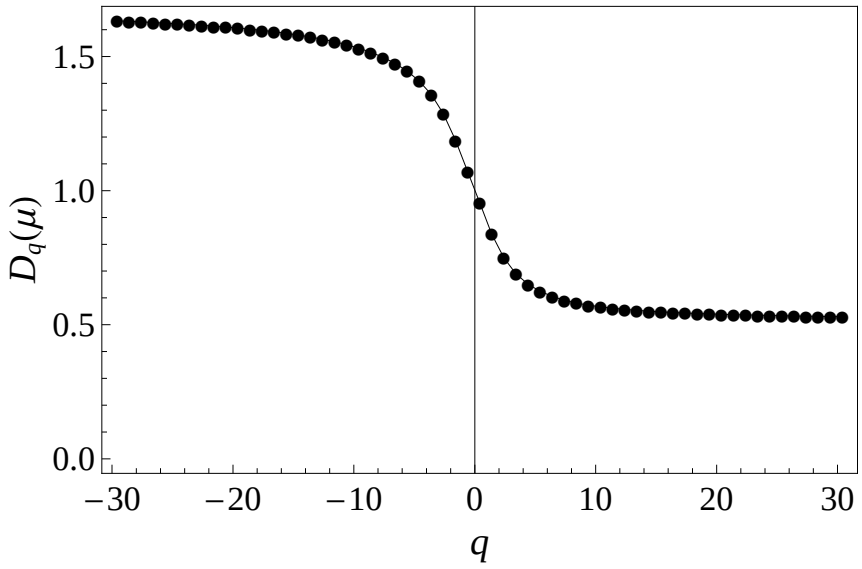

Figure 5.9: The dimension spectrum $D_q(\mu)$ for the extracted measure of a multi-fractal stochastic process.

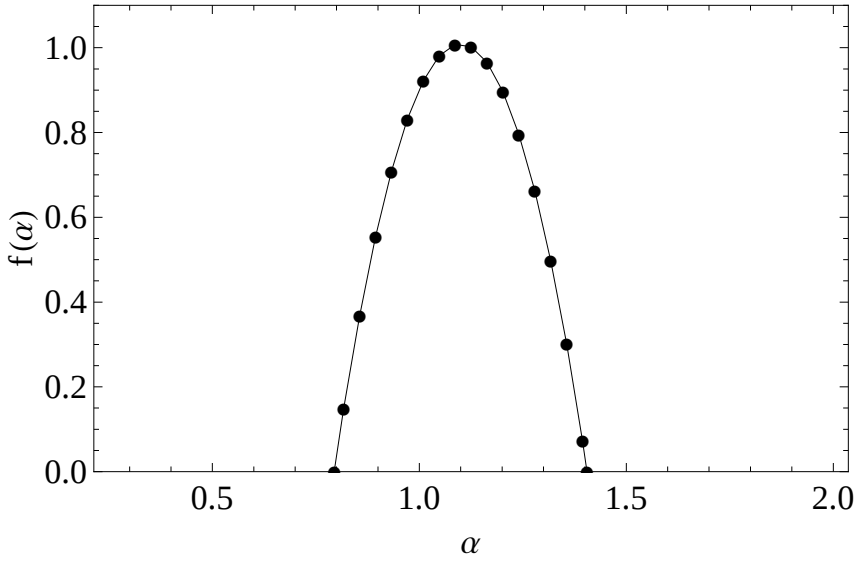

Figure 5.10: The multi-fractal spectrum for the extracted measure of a multi-fractal stochastic process.

Another point of view is to consider the multi-fractal spectrum. In figure 5.10 the spectrum shows appreciable multi-fractality. So far we have mostly considered Bernoulli measures. In figure 5.11 we constructed a process with a Markov measure as the multi-fractal time component. In figure 5.11(a) we see the Markov measure visually having strong similarities to the Bernoulli measure. In fact if $\pi_{11} = \pi_{21}$ and $\pi_{12} = \pi_{22}$ we get the Bernoulli measure. Considering the structure functions of the MMAR-process in (c) and the estimated scaling function in (d) we find the Hurst exponent to be $H = 0.46$. The actual Hurst exponent is $H = 1/2$. We also notice a concave scaling function. So far there is nothing essentially different of what we would get using a simple Bernoulli measure. The mayor differences lies in the construction of the Markov measure where we have to determine more free parameters. In our situation we have a probability matrix

$$\Pi = \begin{pmatrix} \pi_{11} & \pi_{21} \\ \pi_{12} & \pi_{22} \end{pmatrix} = \begin{pmatrix} \frac{1}{4} & \frac{3}{4} \\ \frac{1}{3} & \frac{2}{3} \end{pmatrix}.$$

A comparison of the estimated scaling function with the theoretical scaling function following the relation

$$\zeta_X(q) = 1 - \frac{\log \rho\left(\left\|\pi_{ij}^{Hq}\right\|\right)}{\log 2}$$

is shown in figure 5.12. Our experience is that modeling with a Markov measure requires larger samples to ensure satisfactory results, as compared to Bernoulli measures. It could be of interest to further expanding the Markov measure to higher order measures but this is not discussed in this paper.

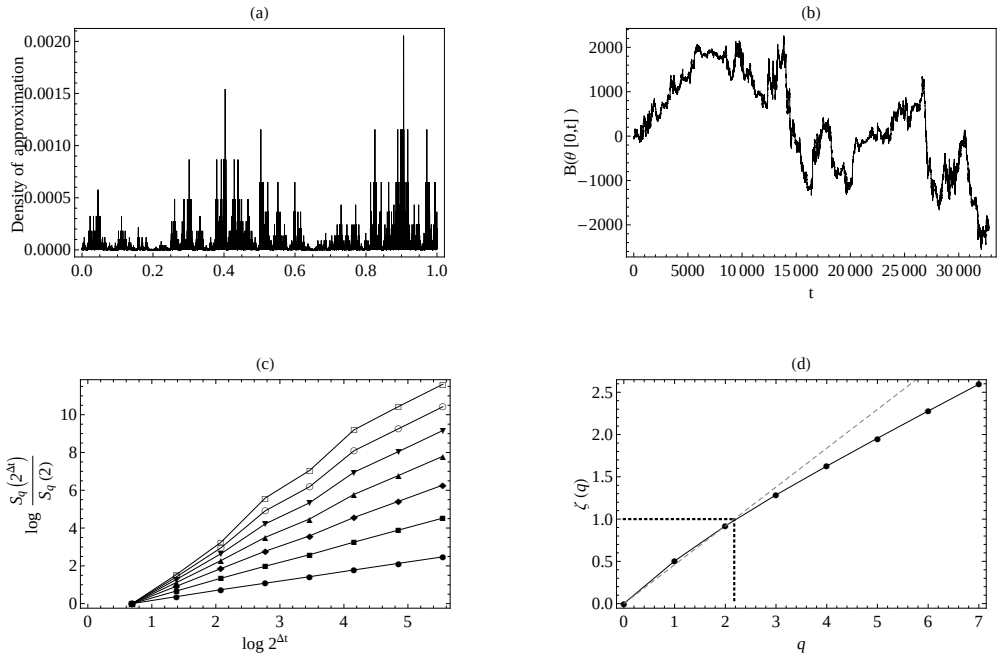

Figure 5.11: (a): Density of approximation to a random measure. (b): Realization of $X(t) = B(\Theta(t))$ where $\Theta(t)$ is the distribution function of a randomized Markov measure. (c): Structure functions of the process. (d): Estimated scaling function of the process and calculation of the Hurst exponent which is found to be $H = 0.46$.

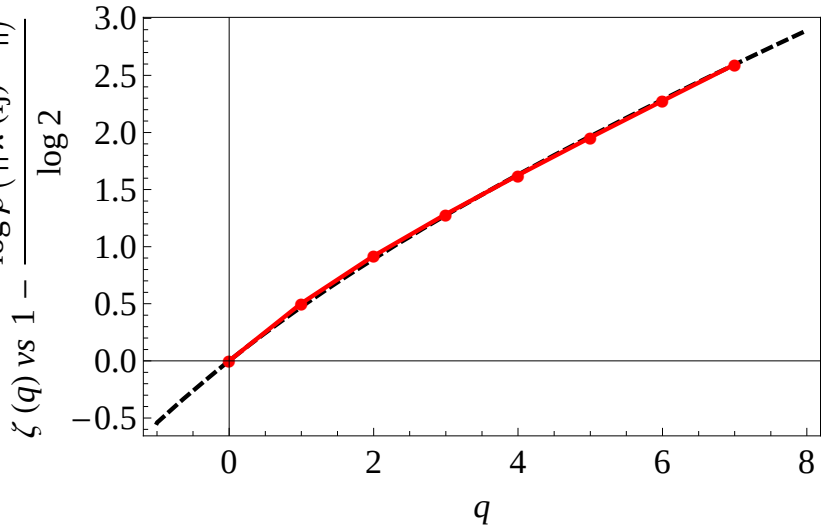

Figure 5.12: Comparing the estimated scaling function of the process and the theoretical scaling function for a process defined by a random Markov measure.

5.2.1 Fractional Brownian Processes as the "outer" process

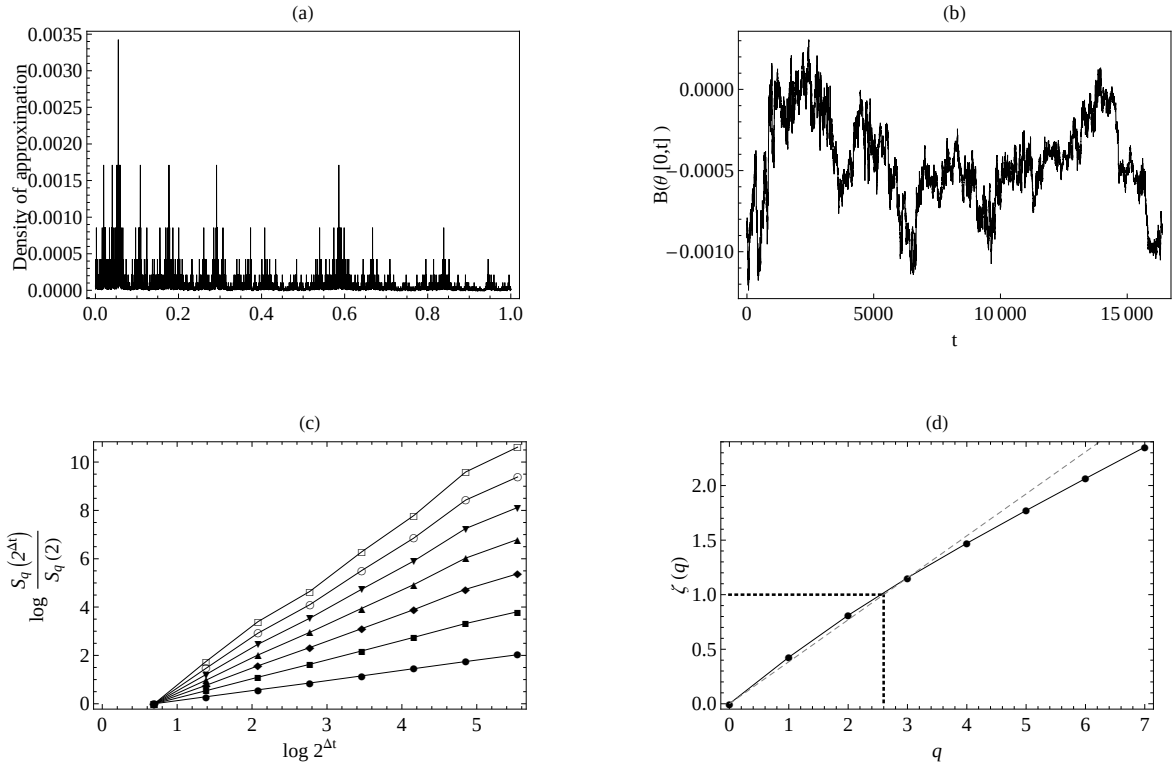

Figure 5.13: (a): Density of approximation to Bernoulli measure. (b): A realization of $X(t) = B_H(\Theta[0,t])$ with $H = 2/5$. (c): Structure functions of the process. (d): The related Scaling function. The Hurst exponent is found to be 0.38. This is close to the actual value $H = 2/5$.

We now consider the case where the "outer" process is a fractional Brownian motion and $\Theta(t)$ is the distribution function of a random Bernoulli measure. In figure 5.13(b) the fractional Brownian motion has $H = 2/5$. The process is constructed from an inverse Fourier method. In figure 5.13(a) the random iterated measure corresponds to the previously discussed Bernoulli measure. As shown in figure 5.13(c) we find the structure functions which give the estimated scaling function in (d). The structure functions are close to linear, making it easy to find linear approximation of the structure functions. In (d) we notice the concave scaling function gives the Hurst exponent $H = 0.38$.

A realization of the process $|X(t+\Delta t) - X(t)|^{\frac{1}{H}}$ where $X(t) = B(\Theta(t))$ is shown in figure 5.14(a). By construction we know the exact measure. This is shown in (b).

In figure 5.15 we compare the distribution functions of the measures of figure 5.14(a). Slight deviations are expected but generally we will conclude it to be a good approximation.

We compare the scaling function of the multi-fractal process with the scaling function of

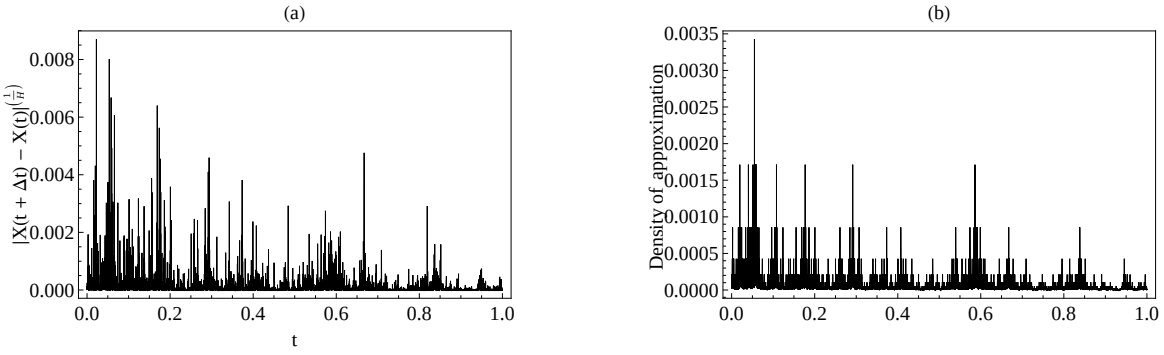

Figure 5.14: (a): The increments of the process at powers of $\frac{1}{H}$ represents the extracted measure. (b): Density of an approximation to the constructed measure.

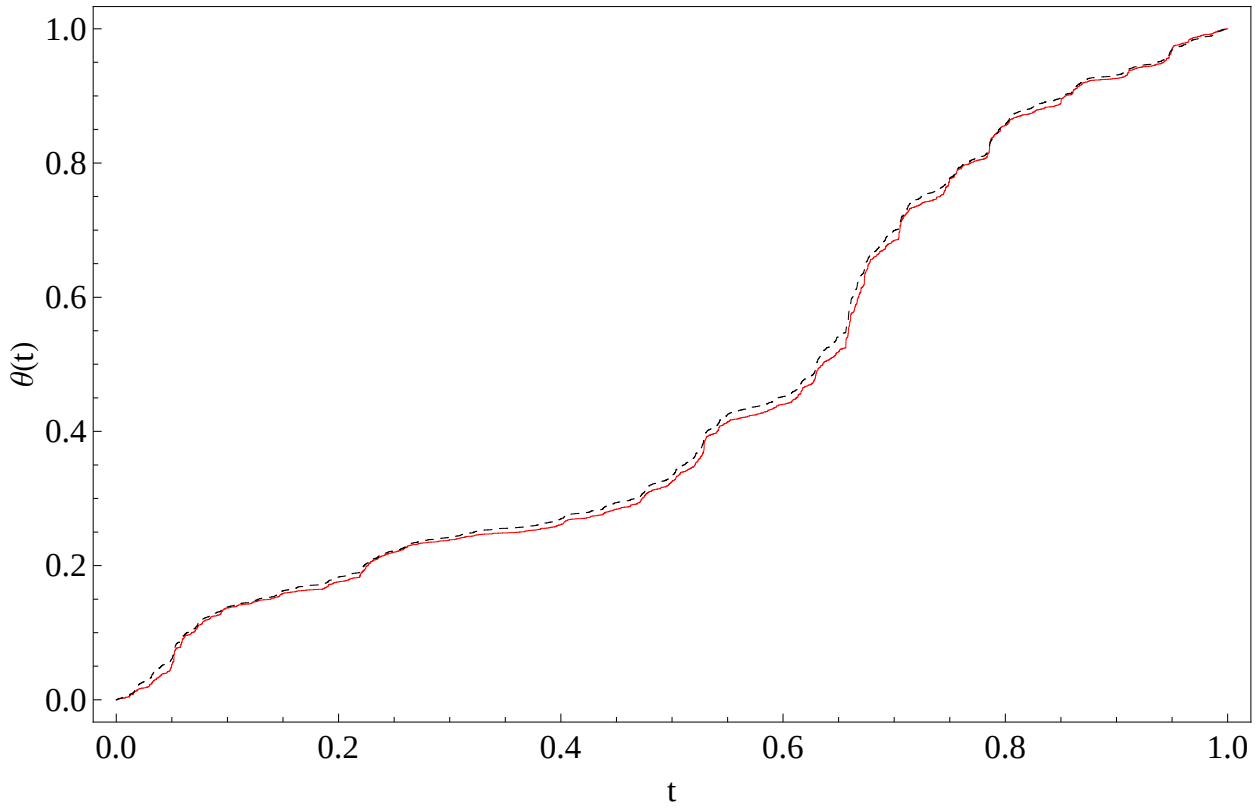

Figure 5.15: Comparisons between the constructed $\Theta(t)$, represented by the dashed curve, and the extracted $\Theta(t)$ of the process, represented as the continuous curve.

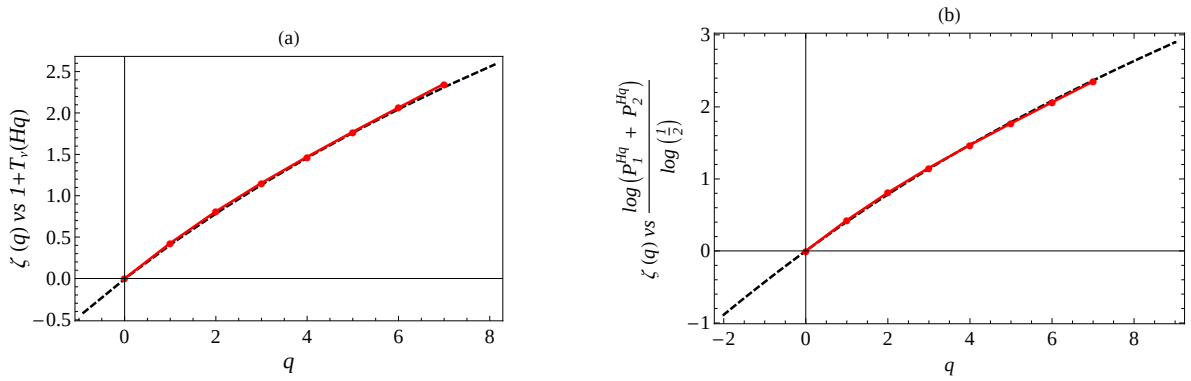

Figure 5.16: (a): The theoretical scaling function, represented as the dashed curve, from the relation $\zeta(q) = 1 + T_\nu(Hq)$. The solid curve that almost overlaps the dashed curve is the scaling function found from the multi-fractal process. (b): The theoretical scaling function of a Bernoulli measure $\left(T_\nu(q) = -\frac{\log(P_1^q + P_2^q)}{\log 2}\right)$ as the dashed curve, and is compared with the scaling function of the multi-fractal process.

the extracted measure following the relation $\zeta_X(q) = 1 + T_\nu(Hq)$ where X is the compound process, and T_ν is the scaling function of the extracted measure. This can be seen in figure 5.16(a). We also compare the scaling function with a the theoretical expression $T_\nu(q) = -\frac{\log(P_1^q + P_2^q)}{\log 2}$. This reveals similar overlapping results as shown in figure 5.16(b). Here we found $P_1 = 0.33$ and $P_2 = 1 - P_1$ which is almost equal to the true probabilities, i.e. $P_1 = 1/3$ and $P_2 = 1 - P_1$.

The spectrum of dimensions of the process reveal the multi-fractality of the process, as is shown in figure 5.17. Figure 5.18 shows a non-trivial singularity spectrum, as is expected from the model. These tests indicate multi-fractal behavior.

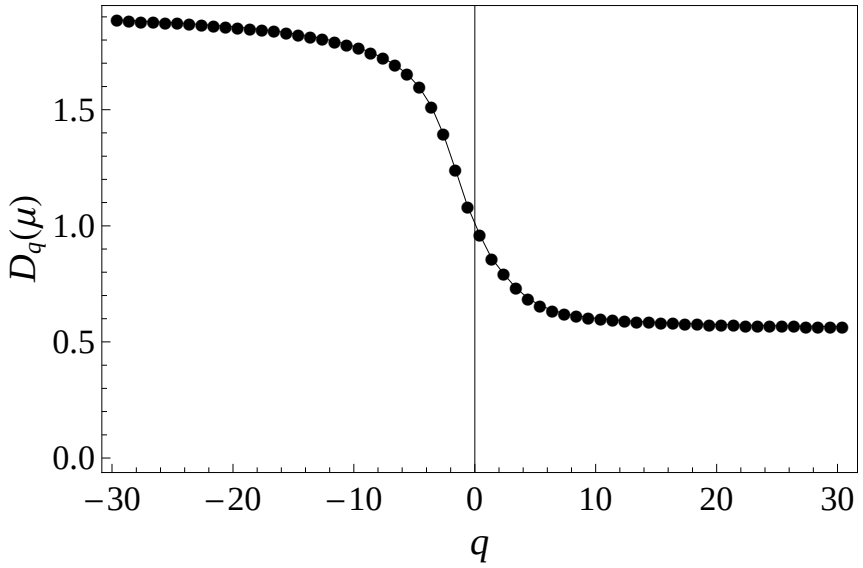

Figure 5.17: The dimension spectrum $D_q(\mu)$ for the process $X(t) = B_H(\Theta(t))$.

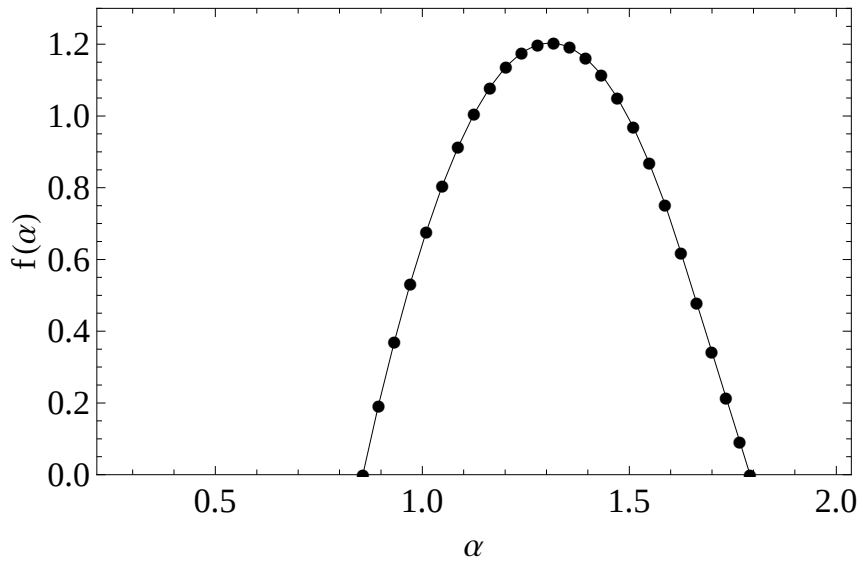

Figure 5.18: The multi-fractal spectrum for the process $X(t) = B_H(\Theta(t))$.

5.3 Modeling Remarks

In several plots of Appendix 6.2 to 6.13 we see structure functions and scaling functions for realizations of different length. It seems that longer realizations tend to give more reliable results. Making statistical statements upon too short realizations will be deceptive.

When modeling we can always compute an estimate for the Hurst exponent and compare with the actual Hurst exponent. In figures (Appendix 6.2 to 6.13) the estimated Hurst exponent was found to vary between 0.47 and 0.54 when the true Hurst exponent is $H = 1/2$. Large deviations between estimated and actual Hurst exponents should encourage us to increase the resolution. This is true especially when considering structure functions of larger order.

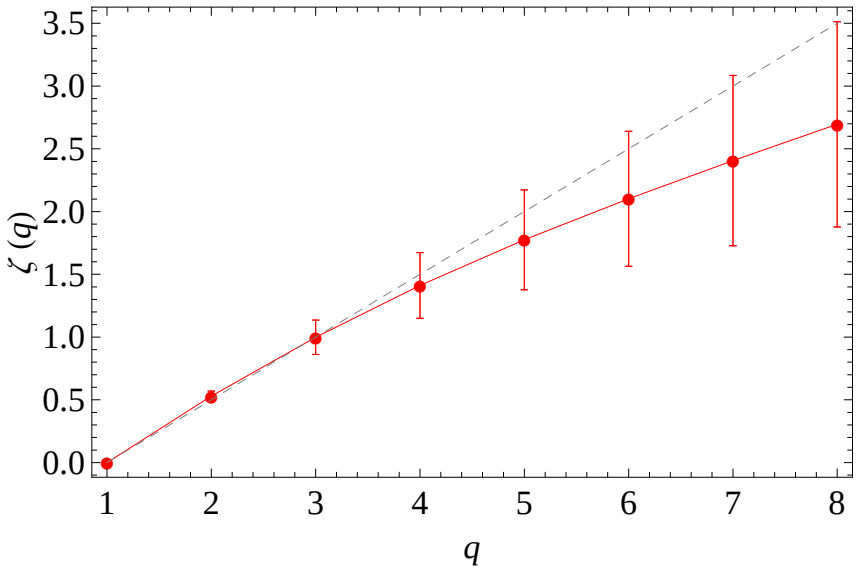

Figure 5.19: Errorbar plot of the scaling function of 20 realizations of a Brownian motion composed with the distribution function of a Bernoulli measure. Each of length 2^{11}. The solid curve represents the average scaling function.

It would be a good approach trying to average several realizations. In figure 5.19 we have 20 realizations of the process. Each of length 2^{11}. The solid concave curve is the estimated average scaling function of the 20 realizations, and as expected gives a rather satisfactory estimate. The error bars represent the greatest departures of the most crooked scaling functions for each q. From this figure 5.19 it would seem questionable to conclude concave behavior since it is possible that the actual scaling might even be linear. For small moments there is little difference between the average and each realization. Naturally higher moments require more data thus giving increasing errors. We would be encouraged to increase the datasets, and in fact this does give much better estimates.

Making a more diversified error plot of several averaged realizations gives an interesting result. As shown in figure 5.20 we see a tendency that the scaling functions are more concave

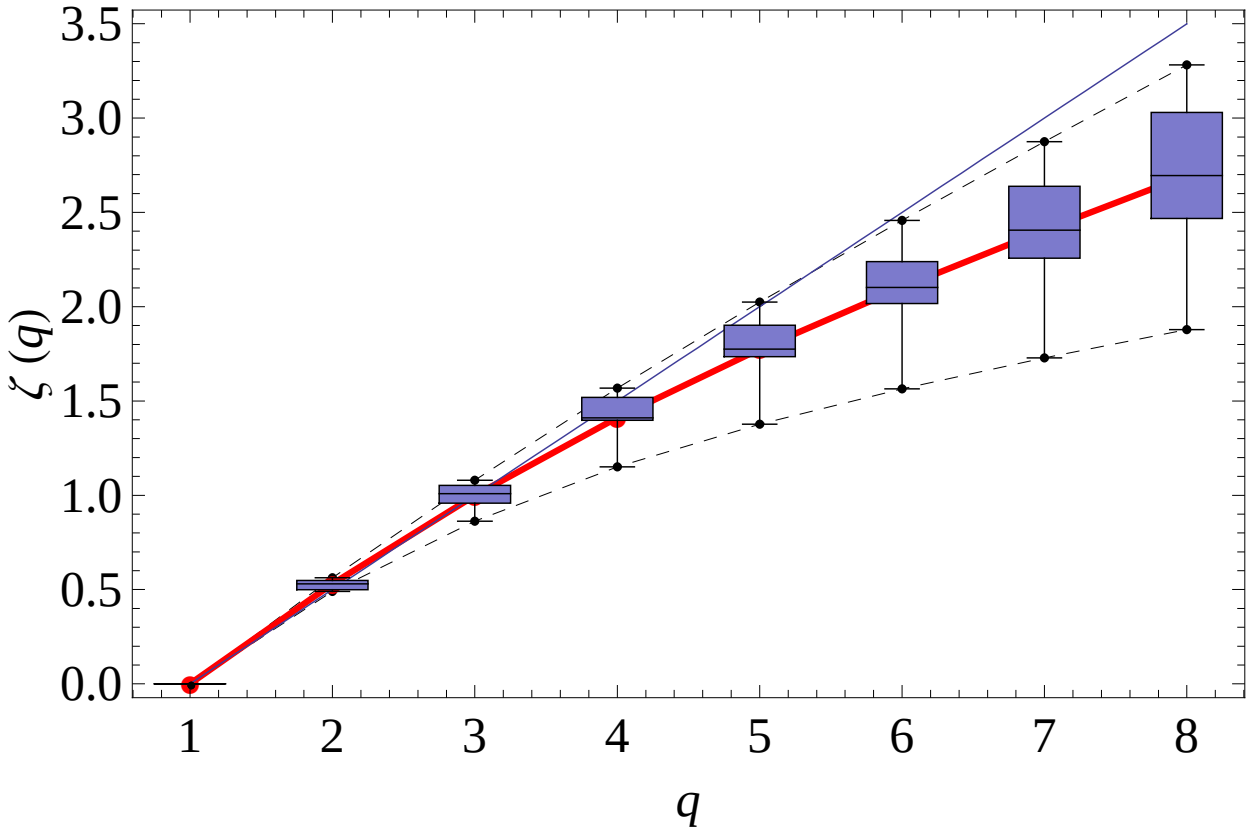

Figure 5.20: Average scaling function over 5 realizations. This is repeated 4 times with box-whisker plots more strictly estimating the extreme values. Each realization is of length 2^{11}.

than contrary. The average scaling function is maintained and most of the realizations are found relatively close to it. The error boxes are box-whisker-plots and are bounded by dashed curves maintaining the greatest deviating scaling function estimates.

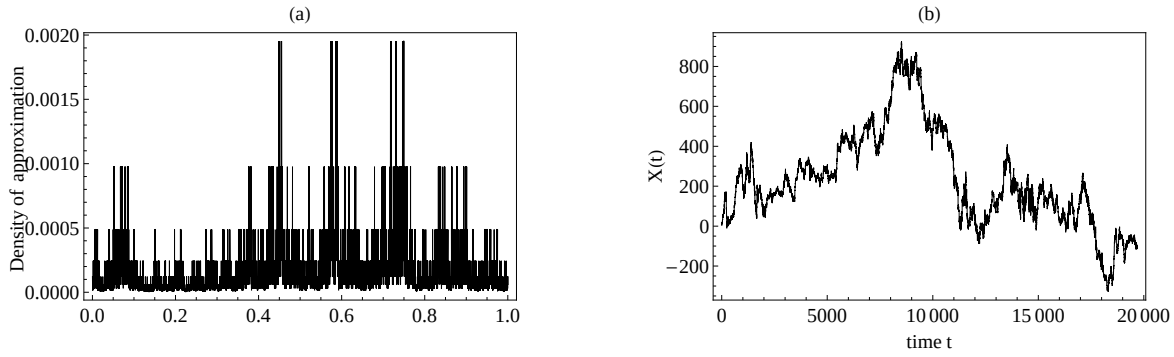

Figure 5.21: (a): Measure constructed with a 3-adic partitioning of the unit interval into subintervals. (b): The corresponding composite process.

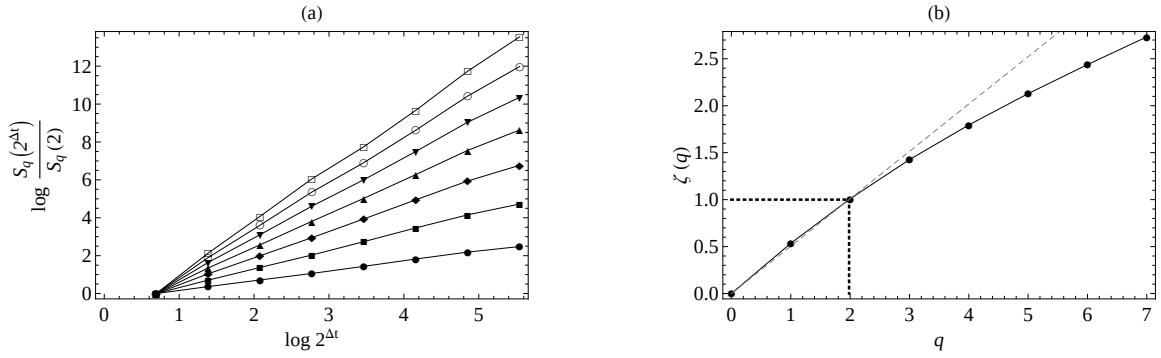

Figure 5.22: (a): Structure functions of the compound process with the 3-adic measure. (b): Scaling function and estimated Hurst exponent $H = 0.51$.

Instead of the dyadic Bernoulli measure one might change the partitioning. A 3-adic partitioning of the unit interval into subintervals at each stage is shown in figure 5.21. It might seem to be good relations between such an approach and the estimated improvements of the structure functions and thus also the scaling function as shown in figure 5.22. Here we got an estimated Hurst exponent of $H = 0.51$ which is reasonable.

Several realizations with this multi-fractal process are averaged in figure 5.23 obtaining the average scaling function. Here each sample path is of length 3^7. The probabilities in the iterated measure are $P = \left\{\frac{1}{4}, \frac{1}{2}, \frac{1}{4}\right\}$. It is noticeable in Appendix figures 6.14 to 6.25 that increasing resolution and number of sample paths influence the estimated scaling

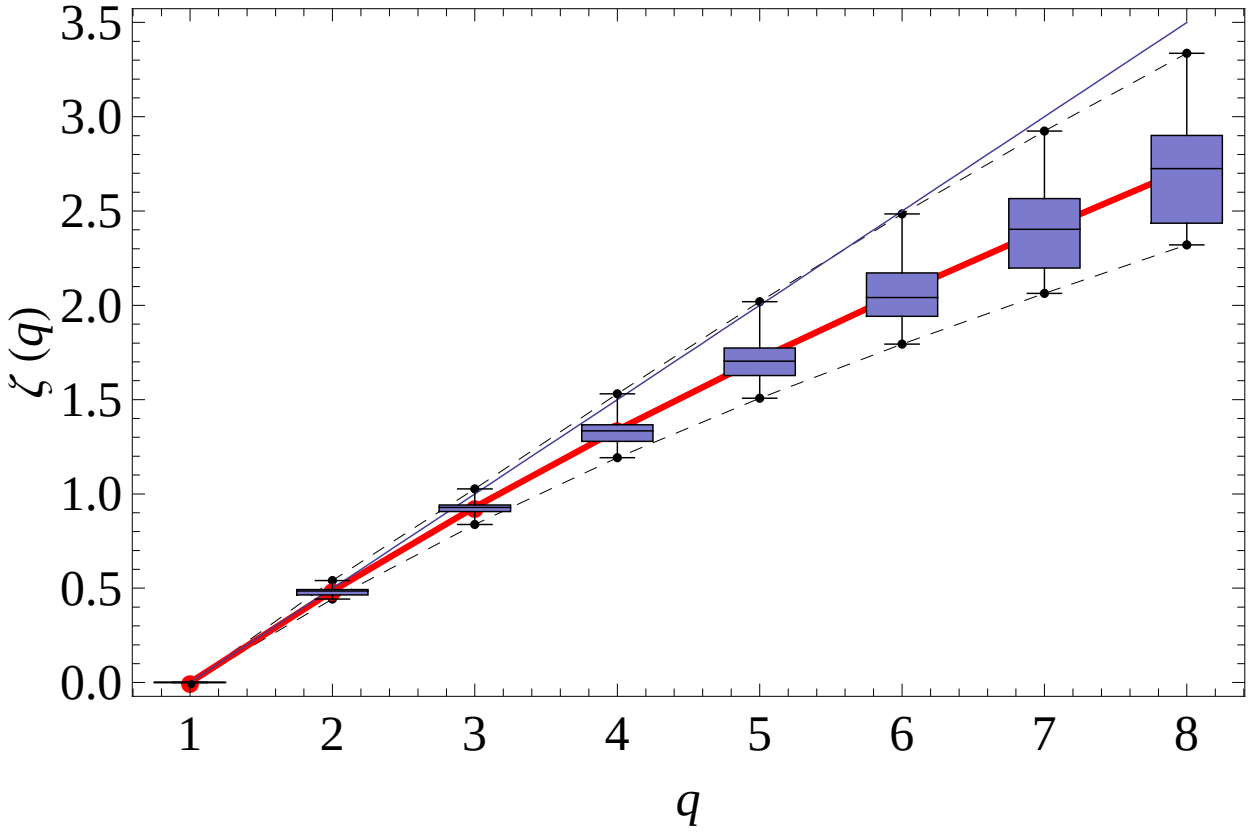

Figure 5.23: Average scaling function over several realizations with box-whisker plots more strictly estimating the extreme values. The underlying process is a composition of a Brownian motion and the distribution function of a 3-adic Bernoulli measure. Each realization is of length 3^7.

function. Generally larger samples tend to ensure improved results. With a higher number of averaged scaling functions the diagnostic tools seems to give good results at the cost of increased computation time. The figures in the Appendix 6.14 to 6.25 consists of several averaged scaling functions.

6 Appendix

IAGA Observatory	Geographic Coord. Code	Lat.(°N)	Geomagnetic Coord. Long.(°E)	Lat.(°N)	Long.(°E)
Abisko	ABK	68.36	18.82	66.04	115.08
Dixon Island	DIK	73.55	80.57	63.02	161.57
Cape Chelyuskin	CCS	77.72	104.28	66.26	176.46
Tixie Bay	TIK	71.58	129.00	60.44	191.41
Cape Wellen	CWE	66.17	190.17	61.79	237.10
Barrow	BRW	71.30	203.25	68.54	241.15
College	CMO	64.87	212.17	64.63	256.52
Yellowknife	YKC	62.40	245.60	69.00	292.80
Fort Churchill	FCC	58.80	265.90	68.70	322.77
Poste-de-la-Baleine	PBQ	55.27	282.22	66.58	347.36
Narsarsuaq (Narssarssuaq)	NAQ	61.20	314.16	71.21	36.79
Leirvogur	LRV	64.18	338.30	70.22	71.04

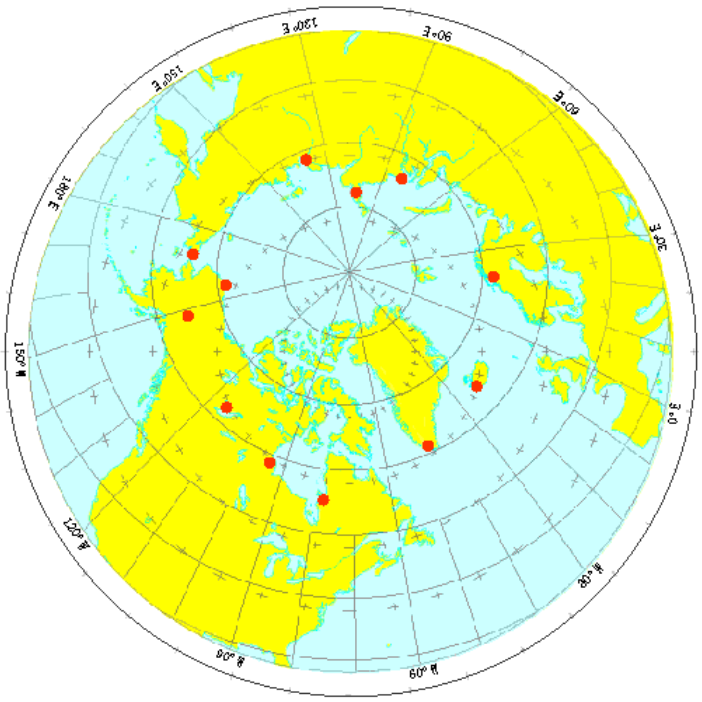

Figure 6.1: The 12 magnetometers deriving AE data by 1992 (2004) [13].

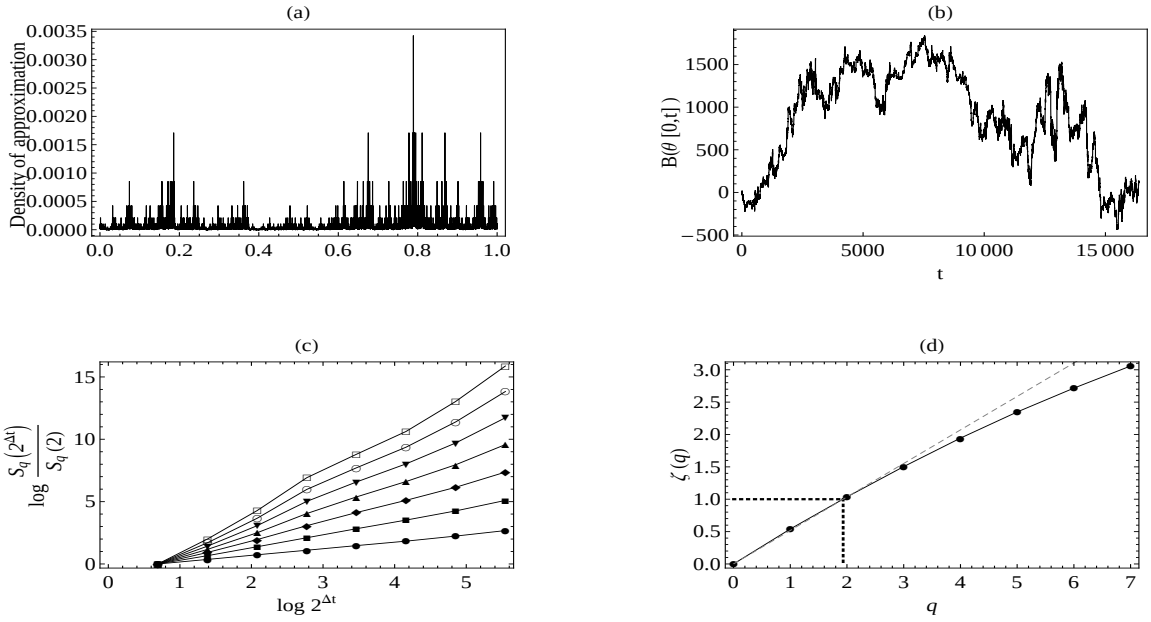

Figure 6.2: (a): Bernoulli measure (b): Brownian motion combined with the distribution function of the measure shown in (a). Number of points: 2^{14} (c): Structure function (d): scaling function

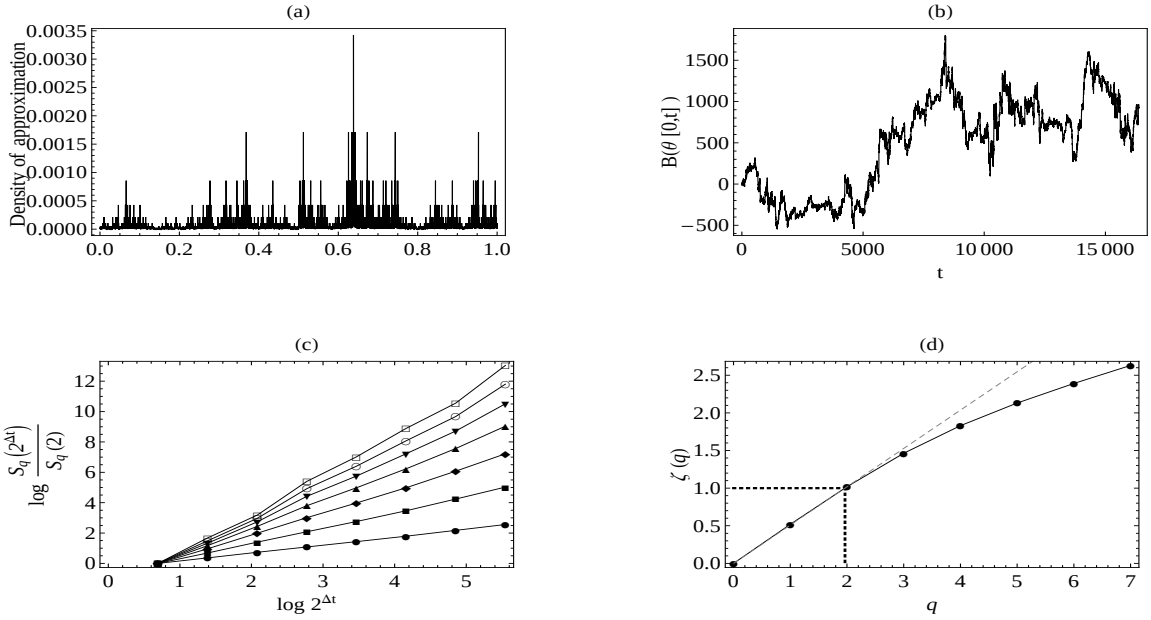

Figure 6.3: (a): Bernoulli measure (b): Brownian motion combined with the distribution function of the measure shown in (a). Number of points: 2^{14} (c): Structure function (d): scaling function

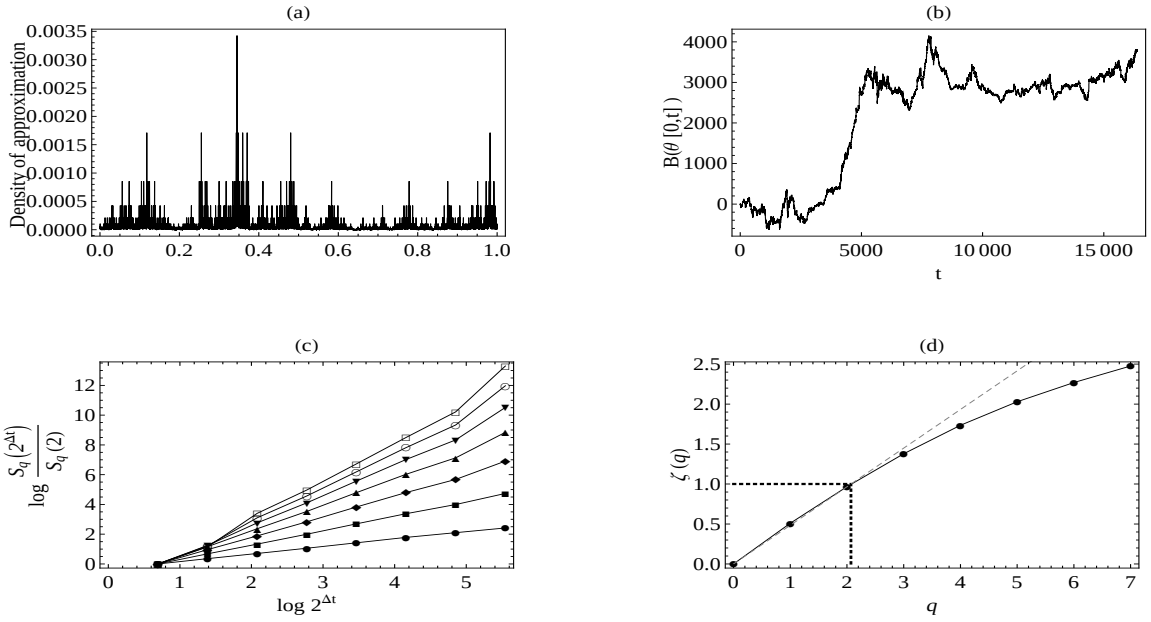

Figure 6.4: (a): Bernoulli measure (b): Brownian motion combined with the distribution function of the measure shown in (a). Number of points: 2^{14} (c): Structure function (d): scaling function

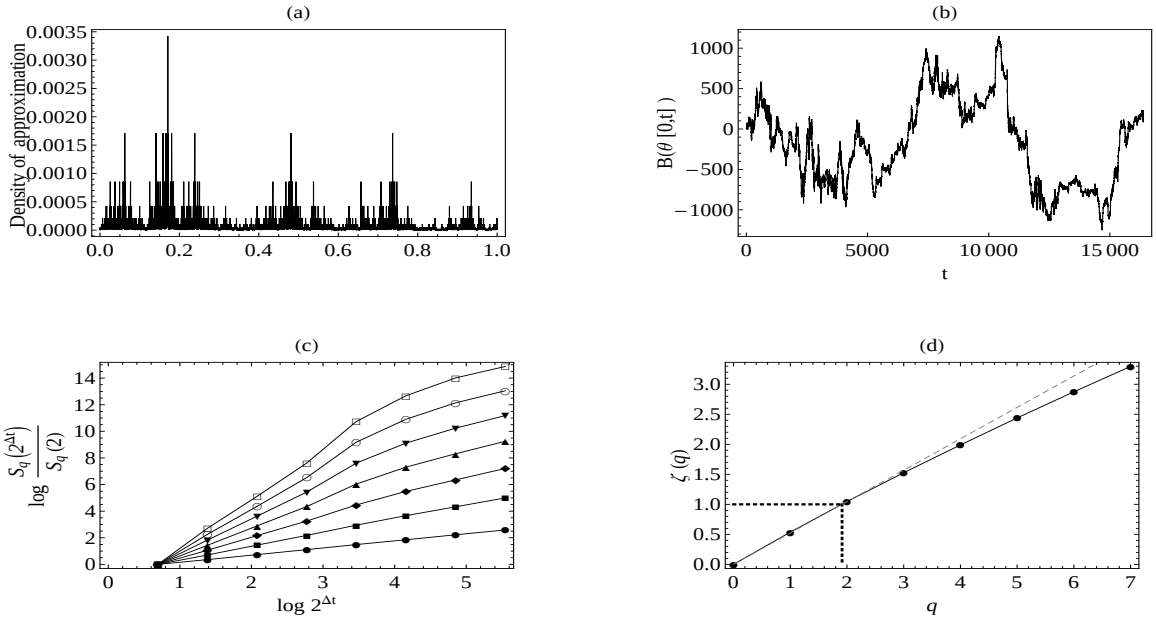

Figure 6.5: (a): Bernoulli measure (b): Brownian motion combined with the distribution function of the measure shown in (a). Number of points: 2^{14} (c): Structure function (d): scaling function

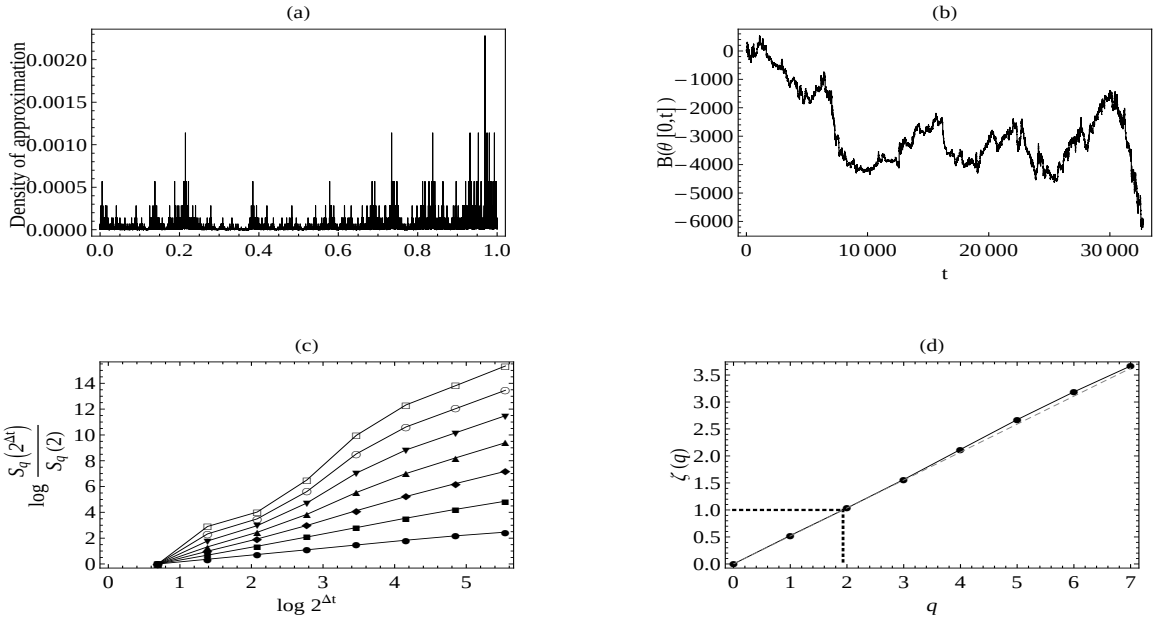

Figure 6.6: (a): Bernoulli measure (b): Brownian motion combined with the distribution function of the measure shown in (a). Number of points: 2^{15} (c): Structure function (d): scaling function

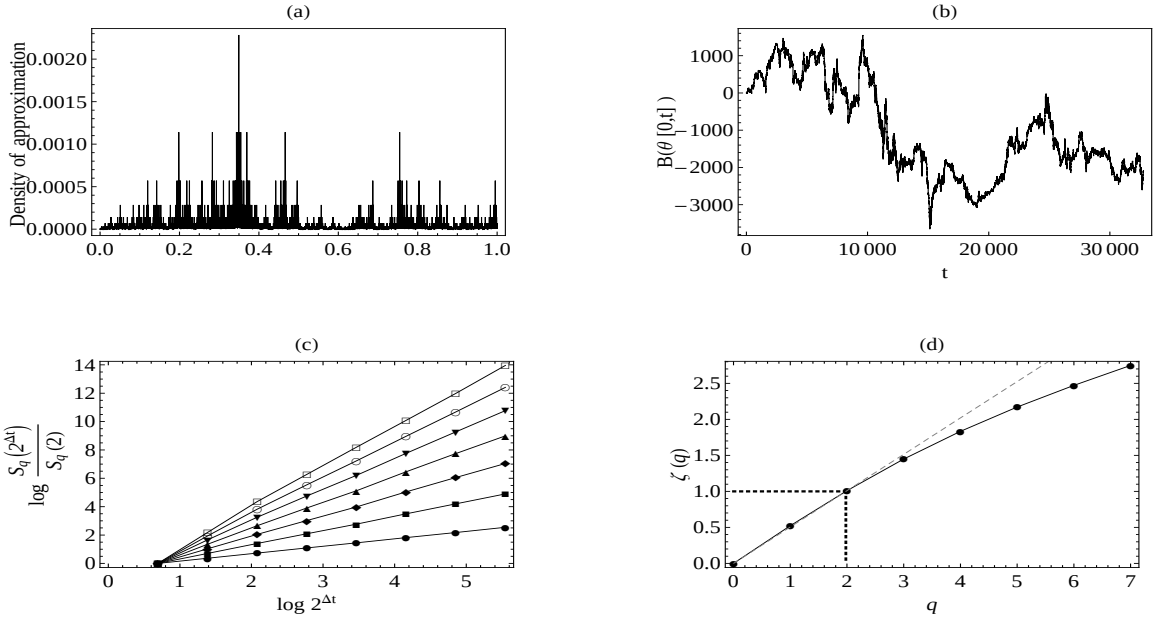

Figure 6.7: (a): Bernoulli measure (b): Brownian motion combined with the distribution function of the measure shown in (a). Number of points: 2^{15} (c): Structure function (d): scaling function

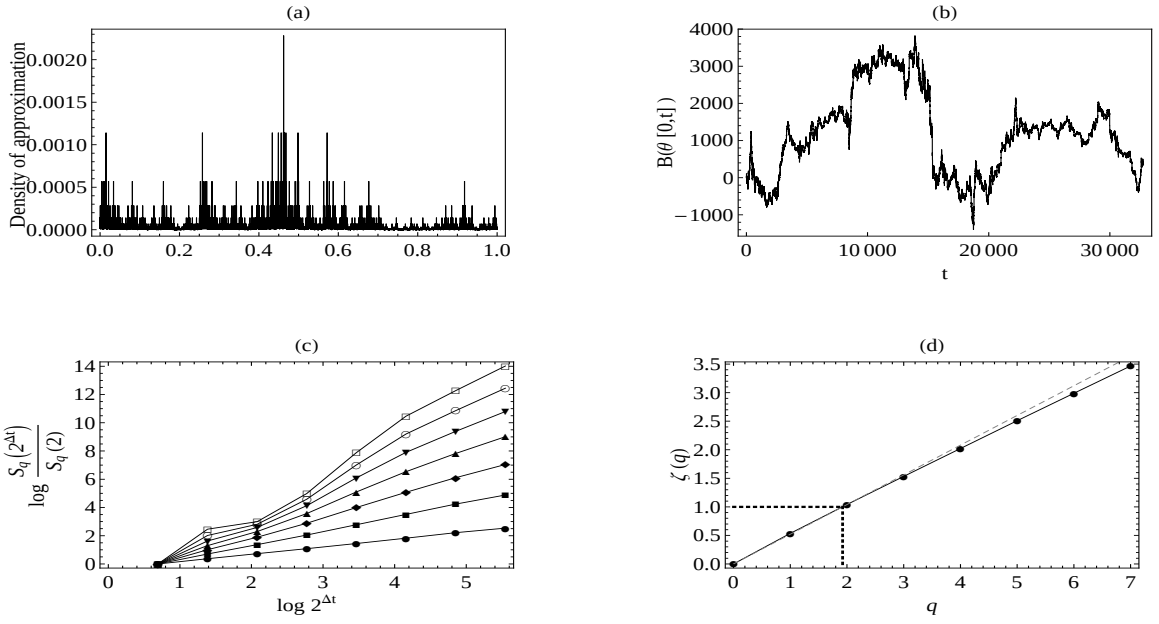

Figure 6.8: (a): Bernoulli measure (b): Brownian motion combined with the distribution function of the measure shown in (a). Number of points: 2^{15} (c): Structure function (d): scaling function

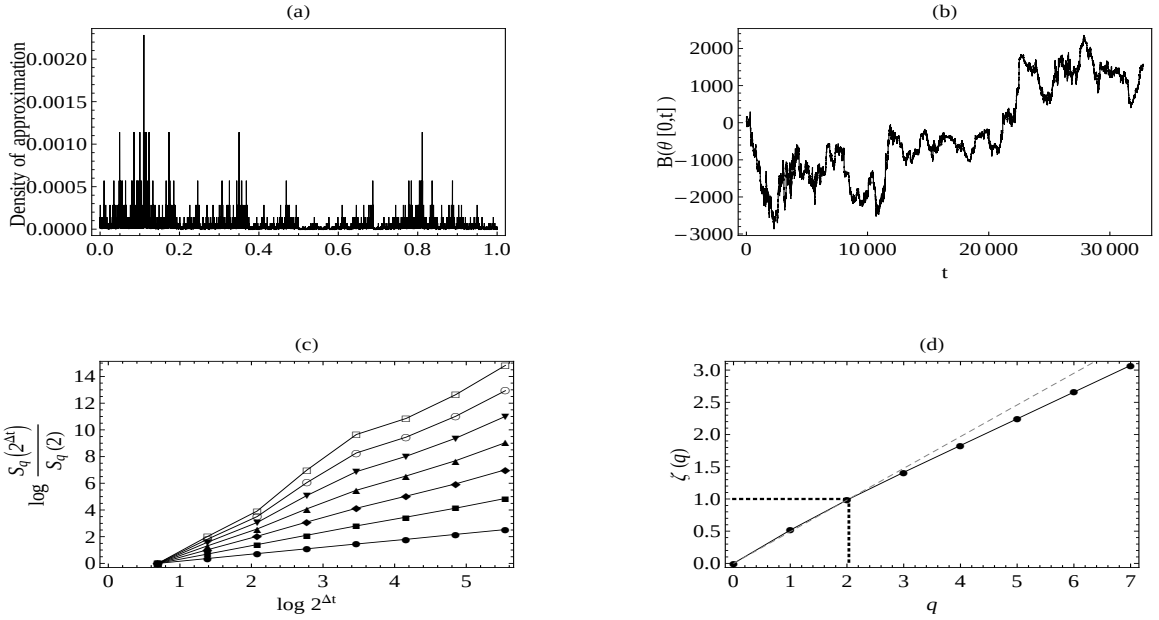

Figure 6.9: (a): Bernoulli measure (b): Brownian motion combined with the distribution function of the measure shown in (a). Number of points: 2^{15} (c): Structure function (d): scaling function

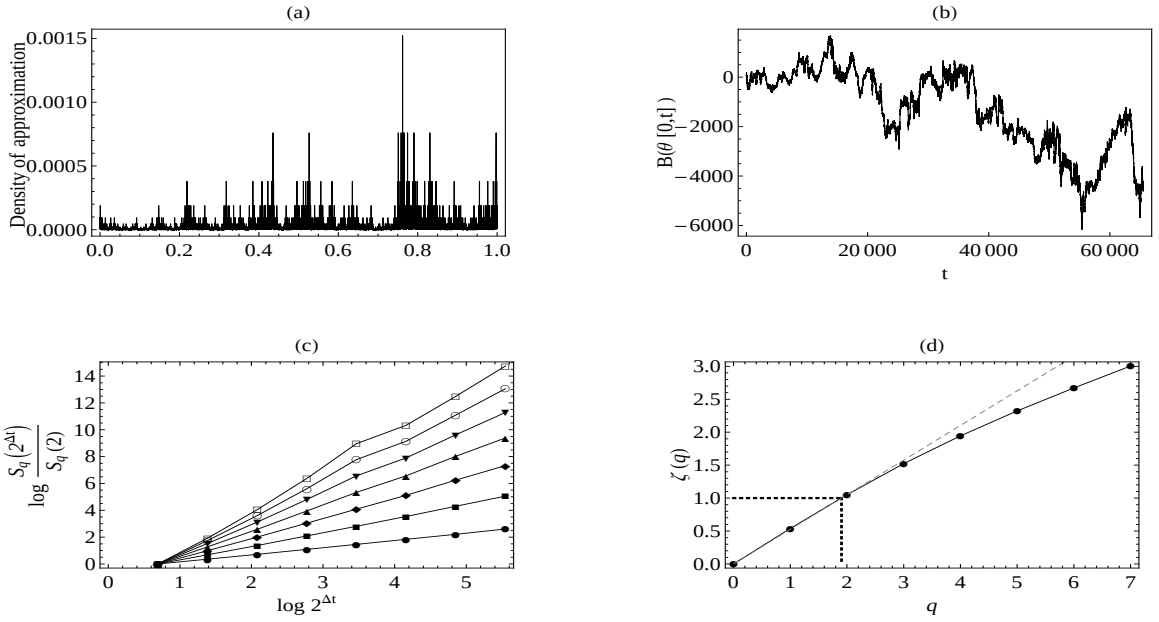

Figure 6.10: (a): Bernoulli measure (b): Brownian motion combined with the distribution function of the measure shown in (a). Number of points: 2^{16} (c): Structure function (d): scaling function

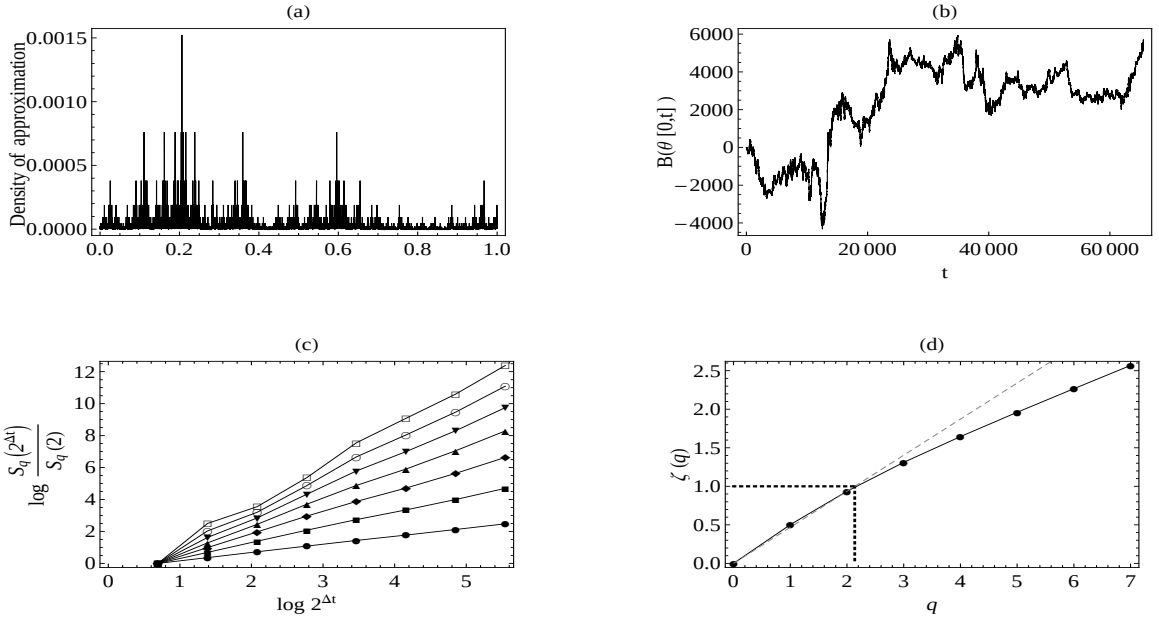

Figure 6.11: (a): Bernoulli measure (b): Brownian motion combined with the distribution function of the measure shown in (a). Number of points: 2^{16} (c): Structure function (d): scaling function

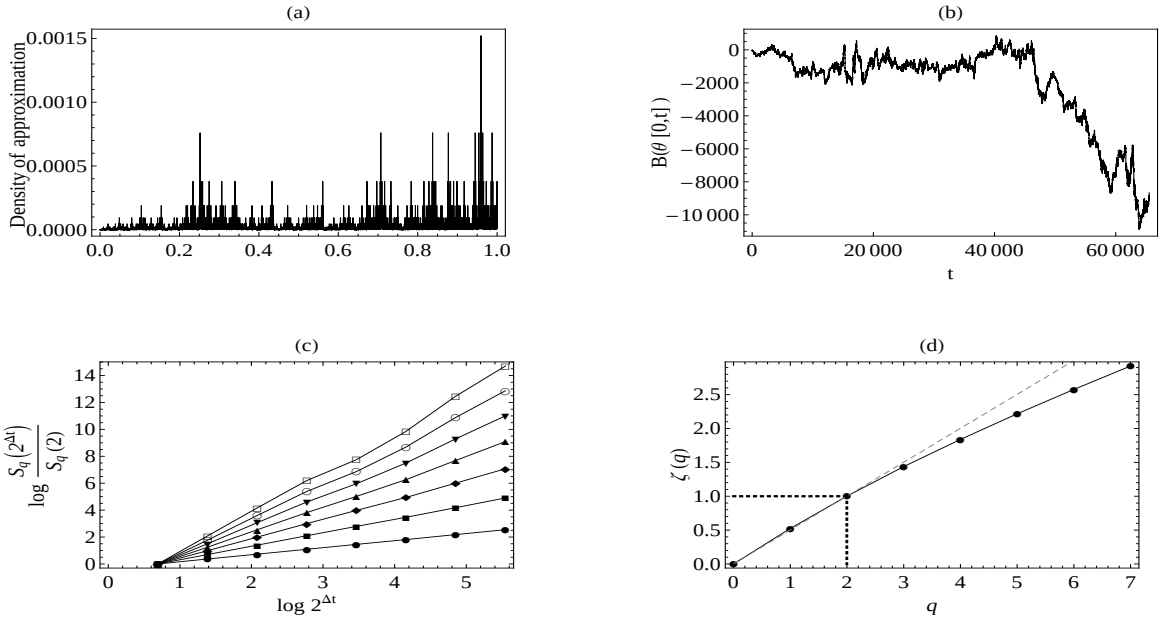

Figure 6.12: (a): Bernoulli measure (b): Brownian motion combined with the distribution function of the measure shown in (a). Number of points: 2^{16} (c): Structure function (d): scaling function

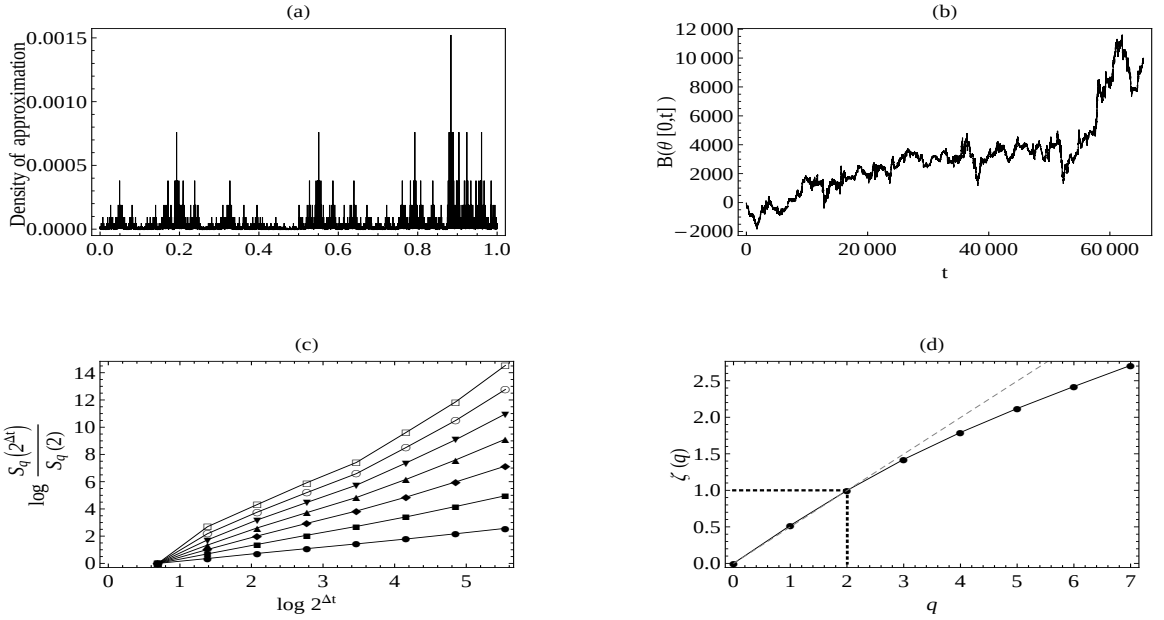

Figure 6.13: (a): Bernoulli measure (b): Brownian motion combined with the distribution function of the measure shown in (a). Number of points: 2^{16} (c): Structure function (d): scaling function

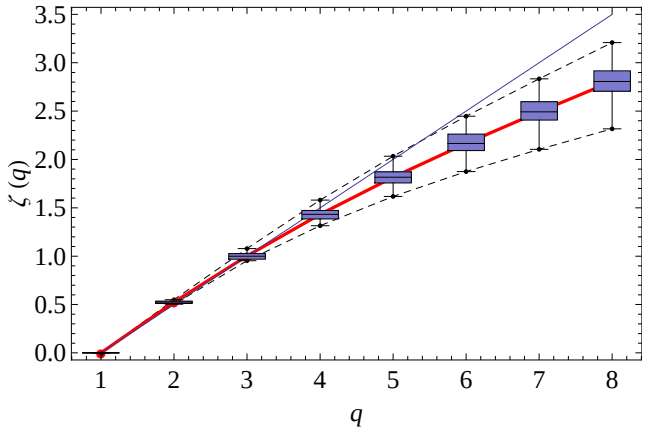

Figure 6.14: Average scaling function of a Brownian motion composed with the distribution function of a Bernoulli measure. Number of points: 2^{11}. Number of repetitions: 40.

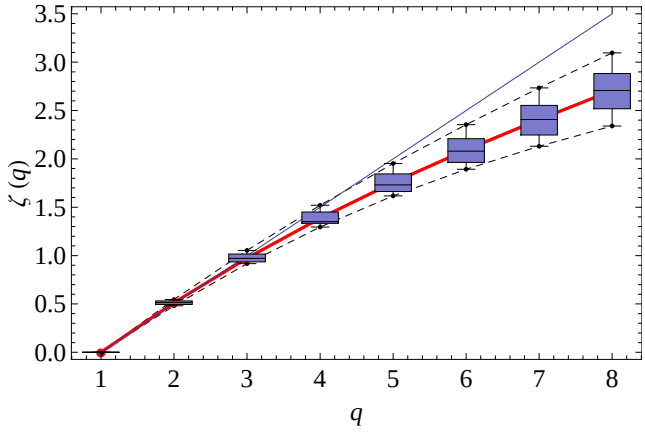

Figure 6.15: Average scaling function of a Brownian motion composed with the distribution function of a Bernoulli measure. Number of points: 2^{12}. Number of repetitions: 40.

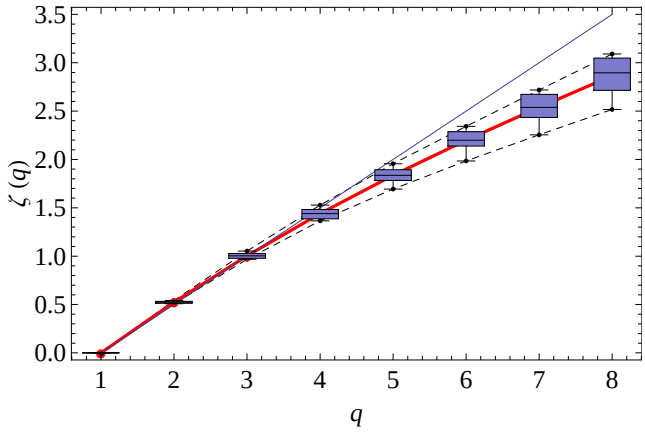

Figure 6.16: Average scaling function of a Brownian motion composed with the distribution function of a Bernoulli measure. Number of points: 2^{13}. Number of repetitions: 40.

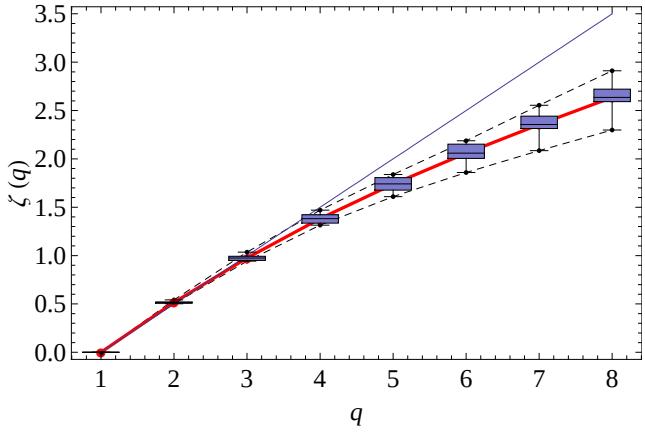

Figure 6.17: Average scaling function of a Brownian motion composed with the distribution function of a Bernoulli measure. Number of points: 2^{14}. Number of repetitions: 40.

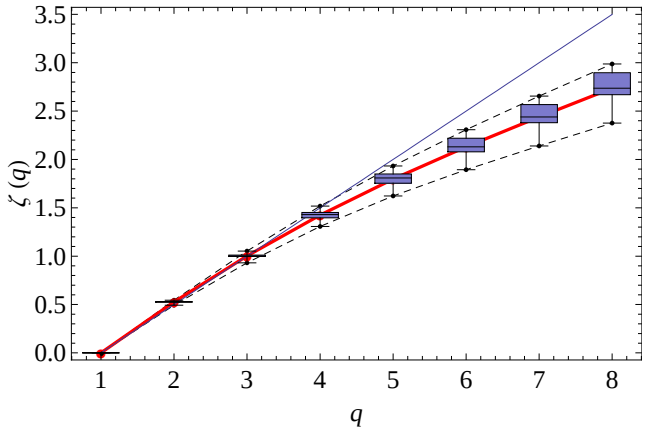

Figure 6.18: Average scaling function of a Brownian motion composed with the distribution function of a Bernoulli measure. Number of points: 2^{11}. Number of repetitions: 100.

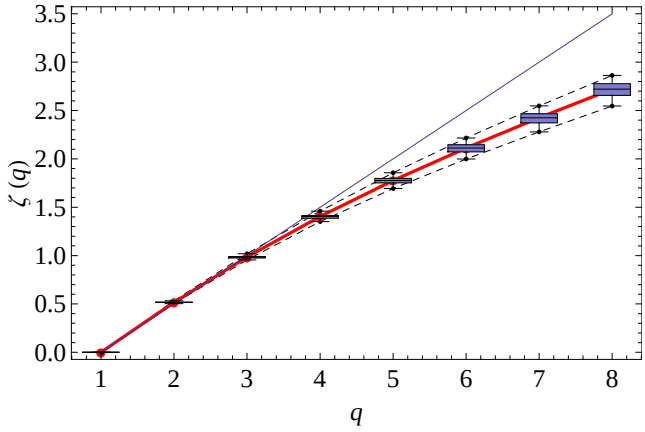

Figure 6.19: Average scaling function of a Brownian motion composed with the distribution function of a Bernoulli measure. Number of points: 2^{11}. Number of repetitions: 200.

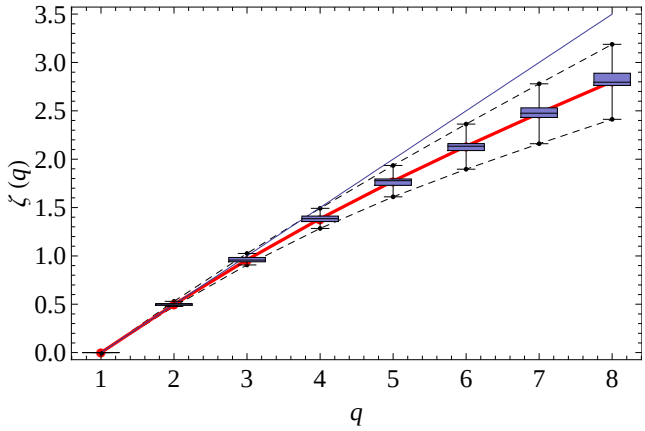

Figure 6.20: Average scaling function of a Brownian motion composed with the distribution function of a 3-adic Bernoulli measure. Number of points: 3^7, with a 3-adic iterated measure. Number of repetitions: 40.

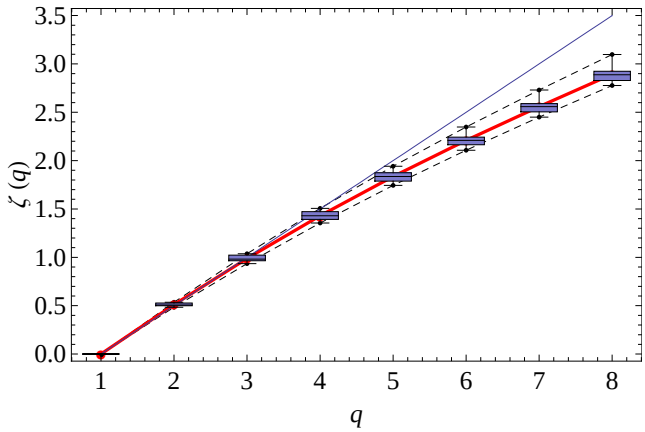

Figure 6.21: Average scaling function of a Brownian motion composed with the distribution function of a 3-adic Bernoulli measure. Number of points: 3^7, with a 3-adic iterated measure. Number of repetitions: 100.

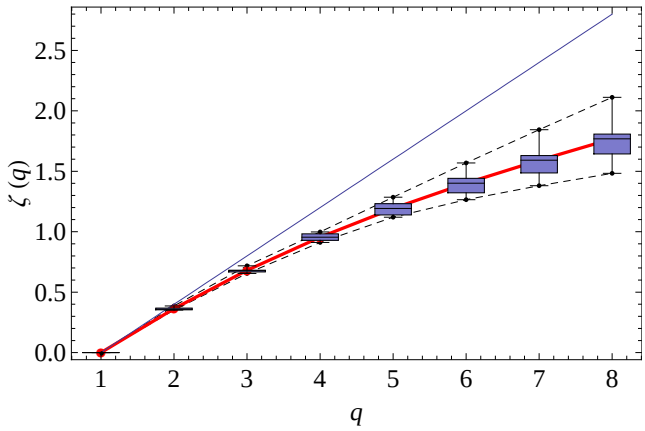

Figure 6.22: Average scaling function of a fractional Brownian motion ($H = 2/5$) composed with the distribution function of a Bernoulli measure. Number of points 2^{11}. Number of repetitions: 40.

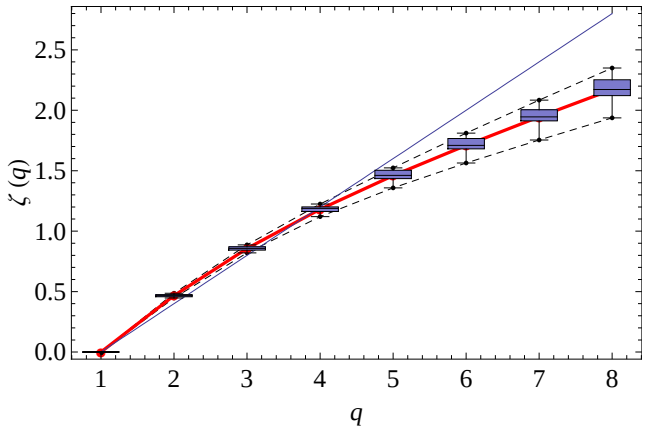

Figure 6.23: Average scaling function of a fractional Brownian motion ($H = 3/5$) composed with the distribution function of a Bernoulli measure. Number of points: 2^{10}. Number of repetitions: 100.

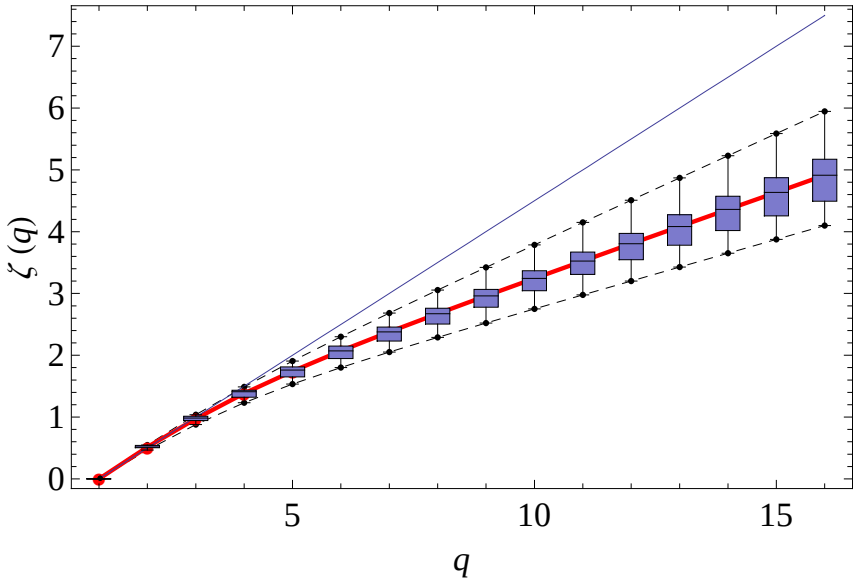

Figure 6.24: Average scaling function of a Brownian motion composed with the distribution function of a Bernoulli measure. Number of points: 2^{11}. Number of repetitions: 40.

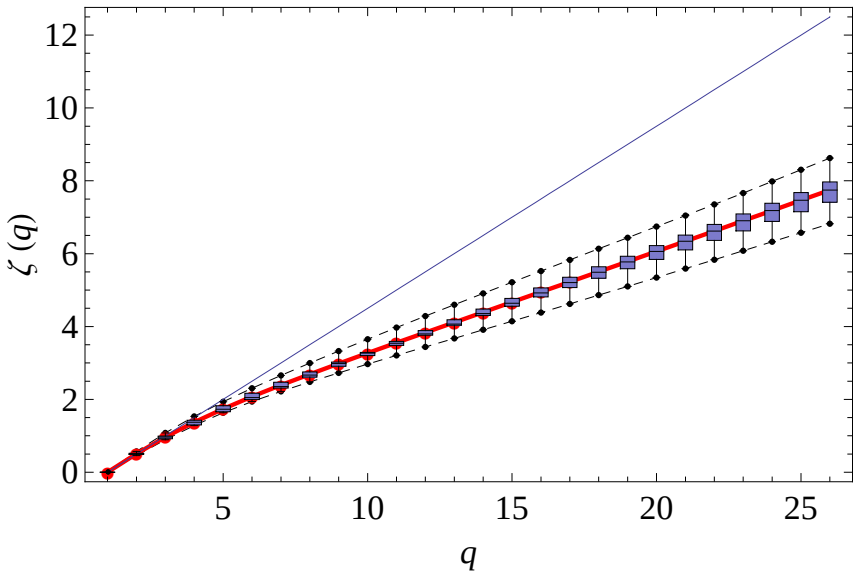

Figure 6.25: Average scaling function of a Brownian motion composed with the distribution function of a Bernoulli measure. Number of points: 2^{11}. Number of repetitions: 70.

References

[1] L. Bachelier. Théorie de la Spéculation, Annales de l'Ecole Normale Supérieure 3. *Paris: Gauthier Villars. English translation in Cootner (1964)*, (1900).

[2] R. T. Baillie, T. Bollerslev, and H. O. Mikkelsen. Fractionally Integrated Generalized Autoregressive Conditional Heteroskedasticity. *Journal of Econometrics*, pages 3–30, (1996).

[3] T. Bollerslev. Generalized Autoregressive Conditional Heteroskedasticity. *Journal of Econometrics 31*, pages 307–327, (1986).

[4] R. Bruno, L. Sorriso-Valvo, V. Carbone, and B. Bavassano. A Possible Truncated Lévy-flight Statistics Recovered from Interplanetary Solar-Wind Velocity and Magnetic-field Fluctuations. *Europhysics Letters, 66(1): 146-152*, (2004).

[5] Wallace H. Campbell. Introduction to Geomagnetic Fields. *Cambridge University Press*, (2003).

[6] G. Consolini, L. Cafarela, P. D e Michelis, M. Candidi, and A. Meloni. Non-Gaussian Probability Distribution of Short Time Scale Magnetic Field Fluctuations at Terra Noa Bay (Antarctica). In S. Aiello, N. Iucci, G. Sironi, A. Treves and U. Villante, editors. *Cosmic Physics in the Year 2000*, SIF Conference Proceedings Volume 58, (1997).

[7] Edwin L. Crow and Kunio Shimizu. Lognormal distributions: Theory and applications. *Marcel Dekker Inc.*, (1988).

[8] R. F. Engle. Autoregressive Conditional Heteroscedasticity with Estimates of the Variance of United Kingdom Inflation. *Econometrica 50*, pages 987–1007, (1982).

[9] Jens Feder. Fractals. *Plenum Press, New York*, Fourth Printing, (1989).

[10] David Fischman. Solar-Terrestrial Physics: Data from Earth's upper atmosphere and space environment to the surface of the Sun, and Earth observations from space. Auroral Electrojet index (AE). *Site: http : //www.ngdc.noaa.gov/stp/*, December (2009).

[11] B. Hnat, S. C. Chapman, G. Rowlands, N. W. Watkins, and W. M. Farrell. Finite Size Scaling in the Solar Wind Magnetic Field Energy Density as Seen by WIND. *Geophysical Research Letters, 29(10)*, (2002).

[12] K. Kabin and V. O. Papitashvili. Fractal Properties of the IMF and the Earth's Magnetotail Field. *Earth Plantes Space 50:87-90*, (1998).

[13] Toyohisa Kamei, Masahisa Sugiura, and Tohru Araki. Data book No 25: "Auroral Electrojet (AE) indices (Provisional AE) 1992" (1998). With additional data support provided at site. *Site: http : //wdc.kugi.kyoto − u.ac.jp/aedir/index.html*, (1992).

[14] B. B. Mandelbrot. Possible Refinements of the Lognormal Hypothesis Concerning the Distribution of Energy Dissipation in Intermitent Turbulence, in: M. Rosenblatt and C. Van Atta eds., Statistical Models and Turbulence. *New York: Springer*, (1972).

[15] Benoit Mandelbrot, Adlai Fisher, and Laurent Calvet. A Multifractal Model of Asset Returns. *Cowles Foundation Discussion Paper no. 1164*, (1997).

[16] Yakov B. Pesin. Dimension theory in dynamical systems: contemporary views and applications. *The University of Chicago Press*, (1997).

[17] Thomas A. Potemra and A. J. Dessler. Space Scientist Honored on Norwegian Currency. *Site: http : //www.fys.uio.no/plasma/english/texts/birkeland/index.html*, (1998).

[18] Sheldon M. Ross. Probability Models. *Academic Press*, (2003). First:(1972).

[19] Martin Rypdal. University of Tromsø lectures in Multifractal Stochastic Processes. Spring (2009).

[20] M. Sund. Project assignment in Industrial Mathematics: Multifraktale stokastiske prosesser. Spring (2009).

[21] Kazue Takahashi, Ching I. Meng, Toyohisa Kamei, Takashi Kikuchi, and Manabu Kunitake. Near-Real-Time Auroral Electrojet Index. *Submitted to Space Weather*, (2004).

[22] J. Takalo, J. Timonen, and H. Koskinen. Correlation Dimension and Affinity of AE Data and Bicolored Noise. *Geophyscial Research Letters, 20(15): 1527-1530*, (1993).

[23] N. W. Watkins, D. Credgington, B. Hnat, and with others. Toward synthesis of solar wind and geomagnetic scaling exponents: a fractional Lévy motion model. *Kluwer Academic Publishers*, (2007).